Experimental observations and statistical modelling of crack propagation dynamics in limestone by acoustic emission analysis during freezing and thawing

Vikram Maji[1,2] and Julian B. Murton[1,3]

[1] Permafrost Laboratory, Department of Geography, University of Sussex, Brighton BN1 9QJ, UK

[2] Experimental Rock Deformation Laboratory, Department of Earth Sciences, IIT Kanpur, Uttar Pradesh- 208016, India

[3]Corresponding author, email: j.b.murton@sussex.ac.uk; ORCID 0000-0002-9469-5856

Vikram Maji: email: vmaji@iitk.ac.in, V.Maji@sussex.ac.uk; ORCID 0000-0003-0870-6625

Key Points

1. Most acoustic emissions occurred during thaw of a limestone block, consistent with microcracking events due to ice segregation.
2. Microcracks propagating outward from the block centre favoured tensional cracking, whereas those propagating inward favoured shearing events.
3. A new microcrack propagation model distinguishes reasonably between cracks formed by volumetric expansion and ice segregation.

Abstract

The timing and location of microcracking events, their propagation and coalescence to form macrocracks, and their development by tension, shearing or mixed modes are little known but essential to understanding the fracture of intact rock by freezing and thawing. The aims of the present study are to investigate the mechanisms and transition of micro- and macrocracking during repeated freeze–thaw, and to develop a statistical model of crack propagation that assesses the

distance and angular relationship of neighbouring cracking events arranged in their temporal order of occurrence. Eight acoustic emission (AE) sensors mounted on a 300 mm cubic block of chalk captured the three-dimensional locations of microcracking events in their temporal order of occurrence during 16 seasonal freeze–thaw cycles simulating an active layer above permafrost. AE events occurred mostly during thawing periods (45%) and freeze-to-thaw transitions (37%) rather than during freezing periods (9%) and thaw-to-freeze transitions (8%), suggesting that most AE (microcrack) events were driven by the process of ice segregation rather than volumetric expansion. The outcomes of a novel statistical model of crack propagation based on two boundary conditions—inside–out and outside–in modes of cracking—were assessed based on Bayes' theorem by testing the hypothesis that the inside–out mode of cracking was favoured by tensional activity, whereas the outside–in mode supported by shearing events. In both situations, the hypothesis accounted for 54–73% confidence level. The microcrack propagation model can distinguish reasonably between cracks formed by volumetric expansion and ice segregation.

Plain language summary

It is well known that repeated freezing and thawing of water within some porous and fine-grained rocks can form large cracks visible to the unaided eye. But the initiation and growth of precursor tiny cracks too small to see without a microscope remain enigmatic in terms of their timing, location, growth and coalescence to form eventually large cracks. Thus, prediction of rock fracture by frost is difficult. Here we present results from a laboratory experiment that measured the location and timing of tiny sound (acoustic) waves within a block of limestone subject to 16 cycles of freezing and thawing. The waves indicated the occurrence of tiny cracking events. Measurement of rock temperature suggested that most cracking events resulted from water migrating through the rock towards lenses of ice rather than expansion of water freezing in place within empty spaces

48 in rock. In addition, cracks propagating outward from the block centre tended to form as the rock
49 was being pulled apart, whereas those propagating inward tended to form by scissor-like tearing of
50 rock. A new statistical model of rock cracking can distinguish reasonably well between cracks
51 formed by growing ice lenses and those formed by expansion of freezing water.
52
53 **Keywords**: Acoustic emissions; freeze–thaw; crack propagation; ice segregation; permafrost

54 1. Introduction

55 Fracture of fine-grained, porous rock by initiation and growth of ice lenses is considered an
56 important mechanism of frost weathering (Matsuoka and Murton, 2008). This fracture process—
57 termed *ice segregation*—refers to migration of premelted water in liquid films through a porous
58 and permeable medium such as soil or rock towards freezing sites, where lenses or layers of ice
59 grow, segregated from adjacent mineral particles and aligned perpendicular to the temperature
60 gradient. Premelting occurs along ice–liquid interfaces, and it enables ice and liquid water to
61 remain in equilibrium at temperatures below 0°C (Dash et al., 2006; Rempel, 2011). Migration of
62 premelted water results from suction induced by temperature gradients within porous media at
63 temperatures below 0°C. Freezing experiments under laboratory conditions indicate that
64 macrocracks can initiate and develop in intact rock, and fill with segregated ice (Agakawa and
65 Fukuda, 1991; Murton et al., 2006, 2016). Less clear are: (1) When and where do the precursor
66 microcracks occur during different stages of freezing and thawing? (2) Do microcracks develop by
67 tension, shearing or mixed modes cracking? (3) How do microcracks propagate and coalesce to
68 form individual macrocracks and pervasively fractured (brecciated) horizons? We hypothesize that
69 tension, shearing and mixed modes of cracking activities of rock vary during different stages of

70 freezing and thawing. We address these questions by monitoring acoustic emissions (AEs)
71 generated by microcracking activity.

72 AEs are transient elastic waves produced by the rapid release of energy from localized sources
73 within a material. AE testing is a non-destructive method for investigating material behaviour based
74 on detection and conversion of high-frequency elastic waves into discrete electrical signals
75 (Goszczyńska et al., 2014). The transducer element in an AE sensor is a piezoelectric crystal that
76 responds with high sensitivity to motion in the low ultrasonic frequency range (10–2000 kHz).
77 When the AE wave front reaches the piezoelectric sensors mounted on the surfaces of a test
78 specimen, minute mechanical movements of the fracture surface molecules are sensed by the
79 transducer and converted to detectable electrical signal. The signal is then amplified and split into
80 discrete waveforms with characteristics such as amplitude, absolute energy, duration and rise time.
81 Multiple piezoelectric sensors arrayed around a structure allow the location of AE activity to be
82 estimated in three-dimensional (3-D) space, based on wave velocity within the material and
83 differences in hit arrival times among the sensors. AE activity has been measured in laboratory
84 freezing experiments with stable thermal boundary conditions (Hallet et al., 1991; Duca et al.,
85 2014). Now it is timely to analyse the changes in AE under dynamic thermal boundary conditions
86 characteristic of natural freeze–thaw cycles.

87 Here we report observations of AE activity monitored during a laboratory experiment on freeze–
88 thaw of limestone. The rationale for the experiment is that 16 freeze–thaw cycles could be carried
89 out over a substantial period of time (470 days) in order to simulate multiple years of an active
90 layer above permafrost developed within a 300 mm cubic block of tuffeau, a type of chalk
91 (limestone) that readily fractures by ice segregation (Murton et al., 2006). Our aims are, first, to
92 investigate the mechanisms and transition of micro- and macrocracking during repeated freeze–
93 thaw, and, second, to develop a statistical model of crack propagation that assesses the distance

and angular relationship of neighbouring cracking events arranged in their temporal order of occurrence. Our objectives are to (1) determine the 3-D location of individual cracking events within the block using multiple AE sensors, and detect and analyze waveforms emitted during them; (2) identify the spatial and temporal distribution, abundance and mechanical characteristics of cracks during different stages of freezing and thawing; (3) distinguish between cracking modes I (tension) and II (shear) during freeze–thaw cycling by parametric analysis of AE waveforms; (4) construct two boundary conditions that reproduce different modes of crack propagation (inside–outward and outside–inward); and (5) compare the patterns of fracture propagation using Bayes' theorem for the two boundary conditions with the tension and shear cracks observed using AEs. The experimental set up and observations of macrocracks, temperature and strain are detailed in a companion paper (Maji and Murton, 2020a) and the freeze–thaw regime is summarized below.

2. Methods

2.1 Freezing and thawing regime

The block of chalk was saturated by capillary rise before starting the experiment and also between its four phases. The block initially froze downward from the top as a result of chilled air circulating in a cold room. Once the block was frozen through, a cooling plate beneath the block was turned on to maintain subzero temperatures in the lower part of the block (simulated permafrost) for the remainder of the experiment. At intervals during the experiment, the chilled air was turned off and the door of the cold room was opened to allow air at ambient room temperature to circulate the cold room and thaw the upper part of the block from the surface downward (simulated active layer). The temperature of the basal cooling plate was thermostatically controlled, with the thermostat set at three progressively higher temperatures during four phases of the experiment (P1–4) in order to simulate active-layer deepening and permafrost thaw during

16 freeze–thaw cycles. The values were set at −15°C for phase 1 (P1: cycles 1–4, days 0–68), −10°C for P2 (cycles 5–8, days 69–203), and −5°C for both P3 (cycles 9–12, days 207–312) and P4 (cycles 13–16, days 315–470) (Figure 1a; Maji and Murton, 2020a). In summary, the experiment consisted of 16 temperature cycles that simulated annual freeze–thaw of a deepening active layer above permafrost.

Each freeze–thaw cycle was divided into four parts. (1) *Thaw-to-freeze transitions* represent the time between imposing a sub-zero air temperature and the onset of more or less isothermal conditions in the frozen chalk block. (2) *Freezing periods* represent the time between the onset of more or less isothermal conditions in the frozen chalk block and the onset of an above-zero air temperature. (3) *Freeze-to-thaw transitions* represent the time between turning off the chilled air supply in the cold room and the development of a stable vertical temperature gradient in the unfrozen simulated active layer. During these transitions the 0°C isotherm descended into the block and stabilized at a certain depth, simulating progressive thaw of the active layer in summer. (4) *Thawing periods* represent the time between the onset of a stable vertical temperature gradient in the unfrozen simulated active layer and the onset of a sub-zero air temperature at the start of the next thaw-to-freeze transition.

2.2 Acoustic emissions

2.2.1 Instrumentation, data acquisition and processing

Eight AE sensors (R-15 alpha, manufactured by Mistras Group) were mounted on five faces of the chalk block (Figure 2). The sensors were distributed using a 3-D Cartesian co-ordinate system to locate single cracking events. Two sensors were mounted diagonally on vertical faces A, B and C, one on vertical face D, and one on the top horizontal surface (to monitor the depth of cracking). A silicon grease epoxy (Pro silicone grease 494-124, from RS Components) was used to establish a

good contact between the smooth ceramic sensor face and the rough vertical rock surface, and a metal cage secured the sensors in place during the experiment (Figure 2d). Two holes (3 mm diameter, ~25 mm long) were drilled into the block to mount each cage, and plastic raw plugs inserted into the holes to anchor the cage with screws. A screw on the top of the cage ensured that the sensors were firmly pressed against the rock faces during the experiment.

The signal from each AE sensor was amplified by a 40 dB gain before processing. Each sensor was connected by a cable 1.5 m long to a preamplifier (IL40S with 32–1100 kHz, Mistras Group) placed inside a box in the cold room. The analog and digital filters used in the preamplifier had ranges of 20–400 and 8–40 kHz, respectively. The preamplifiers were activated by a 28V DC phantom power supply from a PCI Express-8 data card (Mistras Group) installed in a workstation outside the cold room and connected to the preamplifiers by a 10-m-long BNC cable. The layout of the AE data acquisition system is illustrated schematically in Figure 2a.

Data were processed using *AEWin 3D-LOC* software. A threshold of 40 dB was set to separate noise induced in the laboratory from signals of microcracking events. The sampling rate was 1 MHz and the values for peak definition time (PDT), hit definition time (HDT) and hit lockout time (HLT) were 200, 800 and 1000 microseconds, respectively. Every hit captured by the sensors included the parameters amplitude, energy, counts, duration, average signal level (ASL), rise time, average frequency, signal strength and absolute energy.

An AE event was identified if at least four of the eight sensors captured the pulses of energy released (hits). The number of hits and amplitude were considered to eliminate and filter out the noise generated by the freezing system. Data acquisition was continuous throughout the experiment, with a file of AE events produced every 12 hours.

2.2.2 Waveform characteristics

The waveform characteristics obtained from the acoustic waves included the number of hits, duration of the signals, number of counts above a preset threshold (= 40 dB), rise time, amplitude, and energy released (Figure 3a). In order to classify the nature of cracking, the RA value and average frequency were calculated from the waveform characteristics as follows:

$$\text{RA value} = \text{rise time} / \text{maximum amplitude} \quad (1)$$

$$\text{Average frequency} = \text{AE counts} / \text{duration time} \quad (2)$$

These two parameters allowed cracks to be classified as mode I (tension) and mode II (shear) cracks (Figure 3b; JCMS-IIIB5706, 2003; Ohno et al., 2010). The line separating tension and shear events has a slope of 0.1 kHz ms/V following the convention used in JCMS-IIIB5706 (2003). Events lying on the separation line are classified as mixed modes of cracking.

2.2.3 Three-dimensional (3-D) location detection principle

The 3-D locations of AE events were determined—with an additional plug-in code in the *AEWin* software—from the differences in arrival time of acoustic waveforms at sensors that captured any event. This code took into account the array of sensors around the block with respect to a fixed Cartesian reference frame and the velocity of acoustic waves (longitudinal, shear and surface waves) propagating through the material. Hits and events were classified based on their arrival times at four or more sensors around the block. The acoustic wave velocity of the entire block was assumed to remain constant throughout the experiment. This assumption is reasonable when the rock was frozen (i.e., a during the middle to late stages of freezing periods), but during thawing periods slight differences in acoustic wave velocity probably developed between the simulated permafrost and active layer. The 3-D locations of the events within the block were visualized on a graphical interface in *AEWin* and the information was stored for further analysis.

2.3 Statistical model

2.3.1 Theory and mathematical explanation

We developed a statistical model to assess the distance and angular relationships among the temporal order of AE events. The model assumes that the locations and timings of cracking events during the experiment relate to the crack initiation and propagation history observed in the chalk block. The model measures the mean distance and mean angular relationship of the next specified number (N) of consecutive events (N = 2, 5 and 10) relative to each event. The input, throughput and output of the model are illustrated schematically in Figure 4. The model is based on two principal cases of fracture propagation and validated with the AE data recorded in the experiment. The model depicts the best result when N=10, and so we considered N=10 for validation purposes. The model considers the mechanism of crack propagation along the horizontal direction only, because well-developed cracks observed in the block after 8, 12 and 16 freeze–thaw cycles were dominantly horizontal. The model outcomes of the experimental results were correlated with the parametric analysis of the AE waveforms in terms of tension, shear and mixed modes of cracking. Bayesian statistical approaches were incorporated to validate the modelling outcomes on a probability scale.

Two cases of fracture propagation were considered: (1) propagation of cracks from inside the block outward toward the sides, i.e., inside–out (Figure 5), and (2) propagation of cracks from the outer part of the block inward toward the centre, i.e., outside–in (Figure 6). Each case produced a different set of 3-D points containing the locations of the events arranged according to their time of occurrence. The fracture propagation model was then tested on the 3-D location matrices to discriminate the patterns in both scenarios.

$\mathbb{E}n$ is the set containing information about the location of events arranged in their temporal order during any sequence of cracking. It is defined as

$$\mathbb{E}n = \{\xi 1, \xi 2, \ldots\ldots\ldots\ldots, \xi n\} \quad (3)$$

where $\xi 1$, $\xi 2$,…., ξn are the locations of cracking events and can be expressed as $\xi n = [X_n, Y_n, Z_n]$. The fracture propagation mode l$\mathbb{FP}$ assesses the mean distance (r) and mean angular (θ) relationships of a predefined number (N=2,5,10) of next consecutive events and is defined as

$$\mathbb{FP}\ (r) = f\ (\mathbb{E}n) \quad (4)$$

$$\mathbb{FP}\ (\theta) = f\ (\mathbb{E}n) \quad (5)$$

Values of both $\mathbb{FP}\ (\mathrm{r})$ and $\mathbb{FP}\ (\theta)$ of the corresponding events that are far apart indicate events occurred at various locations within the block and can be interpreted as individual cracking events with no definite spatial relationship to each other. Conversely, values of $\mathbb{FP}\ (\mathrm{r})$ of the corresponding events that are close together suggest spatially localized events and may indicate a sequence of cracking. This is true for both distance and angular relationships. $\mathbb{FP}\ (\theta)$ was estimated by converting the location information $\xi 1$, 2, …., ξn into a vector by joining them to the origin, and the angular relationship of events was derived using the dot product of location vectors.

2.3.2 Inside–out crack propagation

The inside–out propagation model assumes that a crack initiated inside the block and propagated outward towards the sides. To evaluate this mechanism against the brecciated layer observed in the experiment (Maji and Murton, 2020a), we considered a definite zone at a depth interval that generated a random set of 3-D numbers representing each AE event. The numbers were generated in order to simulate the inside–out propagation of a crack (Figure 5). As the crack lengthened, the spatial boundary condition of random number generation expanded on the either side, as visualized in Figure 5a. A total of 3000 random points was considered in ten consecutive segments, each with extended spatial boundary conditions relative to the previous one. The 3-D random numbers simulating AE events were restored in a set ($\mathbb{E}_{IO}$) according to their directional order of occurrence. The statistical model was then applied through the simulated event points,

and outcomes of both the angular and distance relationships are presented in Figure 5b–c. The nearest 2, 5 and 10 next consecutive events were considered while performing the statistical algorithm at the initial model construction stage in order to assess the best possible outcome. When the next number of consecutive events was lowest (N=2), the fluctuations in angular and distance values were higher, and when the number was highest (N=10), the curve showed less variation. Both the values of $\mathbb{FP}_{IO}$ (r) and $\mathbb{FP}_{IO}$ (θ) followed a gently increasing trend (Figure 5b–c).

2.3.3 Outside–in crack propagation

The outside–in propagation model simulates a crack originating on two sides of the block within a definite depth interval and propagating inward towards the middle. A similar protocol was applied to create the set ($\mathbb{E}_{OI}$) of locations of events that replicates the outside–in propagation of cracking (Figure 6). The distribution of random events that replicate $\mathbb{E}_{IO}$ is illustrated in Figure 6a. Unlike the inside–out model, in the outside—in model, the results of the statistical algorithm for both situations $\mathbb{FP}_{OI}$ (r) and $\mathbb{FP}_{OI}$ (θ) followed a gently decreasing trend (Figure 6b–c).

2.3.4 Testing the model

Predicted $\mathbb{FP}$ (r) and $\mathbb{FP}$ (θ) values of the statistical crack propagation model, developed by considering the two distinct boundary conditions, were compared with the similar distance and angular variations observed at different depth interval within the specimen during the physical experiment. The observed hypocentres of AE events were spatially grouped into four depth intervals determined from visual analysis of macrocracks and brecciation in the block after 16 freeze–thaw cycles, as described by Maji and Murton (2020a). The AEs in these depth intervals were then filtered and arranged in their order of temporal occurrence following the time stamp recorded during acquisition. The step processing structure of the fracture propagation function is schematically illustrated in Figure 4. The process was repeated for the each of the four depth intervals.

3. Results

3.1 AE activity

AE activity during the four parts of a representative freeze–thaw cycle (freezing period, freeze-to-thaw transition, thawing period and thaw-to-freeze transition) is exemplified from freeze–thaw cycle 5 (Figure 7). The full set of AE activities recorded during all 16 cycles is shown in Supporting Figures S1–S20 and summarized below in terms of their constituent parts.

3.1.1 Freezing periods

Freezing periods had an average duration and standard deviation of 12.68 ± 7.25 days and encompassed 9.46 % of the total number of AE events. AE events were recorded mostly during freezing periods (F) 3–5, with few events during F10 (Table 1; Figures S1–S2). F3–5 occurred during phases P1 and early P2, when the temperature of the air and basal cooling plate was relatively low (Maji and Murton, 2020a).

AE activity clustered mostly around face A during F3–5, with limited clustering around faces C and D (Figure S1: panels 1–4). High-amplitude events (>64 dB) occurred around face A. F10 experienced relatively few events compared to F3–5. In F10, AEs occurred near face B and in the central part throughout the depth of the block, with moderate- to high-magnitude events (56–72 dB) around face B. Moderate- to high-amplitude events were most abundant in the 180–300 mm depth range, although some low-amplitude events (<48 dB) occurred in the upper half of the block (Figure S2: panels 1–4). In F3 and F10, AEs occurred within a short window of time, whereas in F4–5, they continued throughout the freezing period (Figure S1: panels 5–12). In F3–5, the number and magnitude of shearing mode events were higher than those of tension, whereas F10 was dominated by tension mode events (Figure S2: panels 5–12). Overall, comparatively steep freezing

gradients during P1 initiated AE activity near the beginning of the experiment, and as the intensity of freezing fell in later cycles, the frequency of AE activity reduced.

3.1.2 Freeze-to-thaw transitions

Freeze-to-thaw (FT) transitions had a mean duration of 1.5 ± 0.17 days and encompassed 36.98% of the total number of AE events. Substantial AE activity occurred during all 16 FT transitions (Figures S3–S8; Table 2).

In P1, when the thermal gradient was highest, AE events occurred mostly in the lower half of the block (Figure S3: panels 1–4). In FT1, AEs were mostly in the central part of the block, but in FT2–4, they were mostly near vertical faces A and C (Figure S4: panels 1–4). Some moderate- to high-amplitude (64–80 dB) activity occurred during FT1–2 (Figures S5 and S6: panels 1–4). The tension mode of cracking dominated over the shearing mode, and the intensity of shearing gradually decreased during the course of P1 (Figures S7 and S8: panels 1–4).

In P2–3, when the basal thermal protocol was moderate (–10°C compared to –15°C in P1), the modal depth of the frequency distribution of AE events moved upward into the middle of the block (Figure S3: panels 5–12). However, at the onset of restarting the experiment after pauses between P1 and P2, and between P2 and P3, AE activity was concentrated in the lower half of the block, which is also evident in the transition between P3 to P4 (Figure S3: panels 5, 9 and 13). AE events in P2–3 were mostly localized within the block, unlike the clustering of AEs around the faces observed in P1 (Figure S4: panels 5 and 12). Moderate- to high-magnitude events (56–72 dB) were prevalent, though the high amplitudes clustered mostly around the faces. New clustering of events around faces were marked by high-amplitude activity, as observed in FT 1–2 near face A and in FT 9–10 around face B (Figure S4). High-magnitude activity (> 72 dB) was bounded by initiation and follow-up events both in the depth and time domain, as observed in FT1, 2, 6, 10, 11, 13 and 15 (Figures S5

303 and S6). The magnitude of shearing events increased in P2–3, though both tension and shearing
304 modes were abundant (Figures S7 and S8).

305 In P4, AE events occurred throughout the depth of the block and moderate to high-amplitude
306 events were evident (Figure S3: panels 13–16). Both tension and shear modes were abundant.

307 In summary, intense bidirectional freezing coincided with AE activity concentrated in the lower
308 half during P1, whereas higher temperatures in P2–3 coincided with modal AE activity in the central
309 parts of the block. In addition, AEs were localized within the block rather than clustered around
310 faces, though high-magnitude events were localized around faces during P2–3.

311 ### 3.1.3 Thawing periods

312 Thawing periods (T) had an average duration of 13.81 ± 5.38 days and encompassed more AE
313 events (45.37%) than any other parts of the freeze–thaw cycles (Figures S9–S14; Table 3).
314 However, no activity was recorded in T9 and 15.

315 In P1, AE activity mostly occurred in the lower half of the block (Figure S9). The events were
316 highly clustered and isolated around the faces A and C (Figure S10). High-amplitude events (64–72
317 dB) occurred in the upper half of the block (Figures S11–S12). During the entire thawing periods,
318 the tension mode of cracking was of higher magnitude than that of shearing mode. Also, the
319 number of tension events was higher than shearing.

320 In P2–3, the modal depth of AE activity moved higher within the block, similar to that in FT
321 transitions (Figure S9). In addition, abundant events occurred within the block, connecting the
322 clusters developed near the faces during P1 (Figure S10). Faces A and C were mostly connected
323 during P2, whereas faces B and D were bridged in P3. Moderate- to high-amplitude events (56–72
324 dB) occurred in the central and lower parts of the block (Figures S11–S12).

325 In P4, AE events occurred in the middle and lower parts of the block (Figure S10). Clustering of
326 AE occurred around faces, mostly near face D and particularly in the upper half of the block (Figure

S10). Low- to moderate-magnitude events (56–72 dB) occurred in P4 and were concentrated in the middle to lower half of the block (Figures S11–S12).

Overall, high-amplitude events (70–80 dB) were fewer in thawing periods than in freeze-to-thaw transitions. The tension activity was most abundant within the 30–40 (average frequency) kHz window in thaw cycles as compared to freeze-to-thaw transitions, where < 30 kHz events were also recorded. In contrast, freeze-to-thaw transitions recorded higher magnitude shear events than thawing periods (Figures S13–S14).

3.1.4 Thaw-to-freeze transitions

Thaw-to-freeze (TF) transitions had a mean duration of 1.5 ± 0.71 days and encompassed only ~8.17% of the total number of AE events (Figures S15–S20; Table 4). AE activity was greatest in P1–2. Six transitions (TF 1, 6, 10–12 and 16) lacked any AE events.

During P1–2, AE activity occurred mostly in the lower half of the block, whereas in P3–4 very few events were identified (Figure S15). Events mostly clustered around faces A and C, with limited numbers of AEs occurring in the central part of the block (Figure S16). Medium- to high-amplitude events (56–72 dB) were observed in TF2 at ~100–250 mm depth, whereas the rest of the activities were of low to medium amplitude (40–56 dB) (Figures S17 and S19). Both tensional and shearing modes of cracking occurred, with some shearing mode events of high magnitude (Figures S18 and S20).

3.1.5 Summary

Most AE events occurred during thawing periods (~45%) and freeze-to-thaw transitions (~37%), with fewer in freezing periods (~9%) and thaw-to-freeze transitions (~8%). In terms of depth, all AEs (>40 dB), including those of higher magnitude (>60 dB), were concentrated mostly in the lower half of the block in P1, but the modal depth of the events moved upward in P2–3, and events were distributed throughout the block in P4 (Figure 8). In terms of 3-D location, AEs were mostly

clustered and isolated around faces A and C in P1. In P2–4, events were observed in the central part of the block connecting the clusters. However, some new clusters developed around faces B and D during P3 and P4. In terms of magnitude, most events were low to moderate amplitude, though moderate- to high-amplitude events were abundant during P1–3. The modes of cracking were mostly tensional, though abundant shearing activities were recorded. The magnitude of tensional activity was highest in thawing periods. In some instances, however, the magnitude of shearing modes was relatively high in freeze-to-thaw and thaw-to-freeze transitions.

3.2 Crack propagation models at different depth intervals

The experiment formed visible macrocracks at four different depth intervals in the block. These comprise two brecciated horizons at depths of 70–110 mm and 180–220 mm and two horizons with limited numbers of inclined macrocracks at depths of 0–60 mm and 120–170 mm (Figure 9). The brecciated horizons contained mostly horizontal to subhorizontal macrocracks that bifurcated and joined, separating angular and tabular fragments of chalk, and cross-cut by fewer vertical to steeply dipping macrocracks. The lightly cracked horizons above and between the brecciated horizons consisted of single to a few cracks, mostly horizontal to subhorizontal. Further details of the macrocracks are given by Maji and Murton (2020a). First, we describe the timing of aggregated AE events at different depth intervals during the four thermal phases of the experiment, and then we examine the crack propagation models at these different depths.

3.2.1 AE timing during phases 1–4

The timing of AE events in the four depth horizons varied with the imposed thermal boundary conditions (basal cooling thermostat values of −15°C for P1, −10°C for P2, and −5°C for both P3 and P4; Figure 1a). AE events were most abundant in the upper brecciated horizon (70–110 mm depth) during P2–4 (n=273–338) and least abundant in P1 (n=193), when the temperature was lowest (Figure 10). Conversely, events were most abundant in the lower brecciated horizon (180–220 mm

depth) during P1–2 (n=2087–2449), and less common in P3–4 (n=503–828) (Figure 11). In comparison, AEs were most common in the upper horizon of limited fracture (0–60 mm depth) during P3–4 (n=158–273), and less common in P1–2 (n=89–94) (Figure 12). Finally, AEs in the lower horizon of limited fracture (120–170 mm depth) were most common in P2 (n=1507) and least common in P1 and P3–4 (n=437–693) (Figure 13).

3.2.2 Brecciated horizons

Both brecciated horizons decreased overall in the values of $\mathbb{FP}$ (r) and $\mathbb{FP}$ (θ) during the experiment, especially during the first phase (P1). In P1, $\mathbb{FP}$ (r) decreased from ~160 to ~80 mm at 70–110 mm depth (Figure 10b) and from ~180 to ~50 mm at 180–220 mm depth (Figure 11b). Respective drops in $\mathbb{FP}$ (θ) in P1 were from ~50 to ~30° (Figure 10b) and from ~50 to ~20° (Figure 11b). The transition between P1 and P2 marked with a sharp increase in both $\mathbb{FP}$ (r) and $\mathbb{FP}$ (θ), whereas, the values continued to decrease during P2 in both the brecciated horizons (Figures 10b and 11b). Both parameters tended to fluctuate, sometimes substantially, during P3–4, where the amount of oscillation surpassed the overall trend. The highest number of AE events was observed at 180–220 mm depth. AE activity was particularly common during thawing periods and FT transitions in P1–2, though substantial activity also occurred during freezing periods in P1, when the thermal boundary condition was at its lowest (Figures 10c and 11c). At both depth intervals, the majority of cracking events were of shearing mode in P1 and P2, and of tensional mode in P3 and P4 (Figures 10a and 11a).

3.2.3 Horizons of limited fracture

AE activity was least within the shallow horizon of limited fracture (0–60 mm depth, Figure 12), whereas the deeper horizon of limited fracture (120–170 mm depth) showed the second highest AE activity (Figure 13). During P1–2, the values of $\mathbb{FP}$ (r) and $\mathbb{FP}$ (θ) declined overall at 120–170 mm depth (Figure 13b), whereas no obvious trends occurred in either parameter at 0–60

399 mm depth (Figure 12b). The maximum fluctuation in $\mathbb{FP}$ (r) and $\mathbb{FP}$ (θ) at 120–170 mm depth
400 corresponds to 140 mm and 32°, respectively (~190 to ~50 mm and 47–15°) and 40 mm and 40°
401 (~80 to ~40 mm and 50–10°), and at 0–60 mm depth to 60 mm and 16° (~150 to 90 mm and
402 33–17°) and 90 mm and 45° (~200 to ~110 mm and 50–5°) during P1–2. During P3–4 the overall
403 changes in both the values of $\mathbb{FP}$ (r) and $\mathbb{FP}$ (θ) were low at both the depth intervals (Figures 12–
404 13b), and both parameters experienced occasional variation, sometimes substantial. The AE events
405 occurred mostly during the freezing periods in P1 and during thawing periods in P2. In contrast, the
406 events were mostly developed during thawing periods followed by FT transitions in the upper
407 horizon during P3-4, whereas the order was reversed (i.e., FT transitions followed by thawing
408 periods) in the lower horizon. The majority of fracturing activity was of shearing mode in P1 and
409 tension mode in P2–4 (Figures 12–13a).

410 ## 4. Discussion

411 No additional mechanical loading was imposed during the experiment and the fractures
412 developed purely under dynamic thermal boundary conditions. Cracking of rocks under repeated
413 freezing and thawing tends to be slower than that under mechanical loading, and so a long
414 experiment (470 days) with 16 freeze–thaw cycles was required to produce well-developed crack
415 surfaces in a relatively soft limestone. The slow development of cracks—monitored using AEs—
416 elucidates the timing of AEs during freeze–thaw cycles, the depth of AEs and macrocracks, and the
417 modes and mechanisms of cracking. In turn, this permits evaluation of a new statistical model of
418 crack propagation and assessment of the practical significance of distinguishing between cracks
419 formed by volumetric expansion and ice segregation.

4.1 Timing of AE events during freeze–thaw cycles

The timing of AE events within the four parts of each freeze–thaw cycle suggests that the majority of AEs did not result from microcracks formed by volumetric expansion but instead from ice segregation. The maximum number of AE events (45.37%) occurred during thawing periods, followed by freeze-to-thaw transitions (36.98%), even though the average duration of the transitions was only 1.5 days. The fewest AE events were observed during freezing periods (9.46%) and thaw-to-freeze transitions (8.17%). Collectively, this timing suggests that the large majority (>82%) of microcracking events was not associated with rock freezing but instead with rock thawing (during the earlier stages of thawing periods and during freeze-to-thaw transitions) or unchanging thermal conditions (during the later stages of thawing periods). Therefore, we discount volumetric expansion—which is predicted to occur in bursts during rock freezing, as liquid water freezes and expands (Walder and Hallet, 1986)—as the main cause of AEs. We conclude that most AEs resulted from ice segregation. The process of ice segregation is expected when temperature-gradient-induced cryosuction draws liquid water to ice bodies within cracks (Taber, 1930; Walder and Hallet, 1986), which may arise as rock thaws or freezes. However, we cannot discount volumetric expansion as a cause of AEs during freezing periods or thaw-to-freeze transitions. For example, in freezing periods, AE activity was mostly limited to P1, which implies that for the lowest basal temperature regime (i.e., –15°C and lower), AEs were caused by volumetric expansion as the low temperature led to rapid freezing of pore water within the chalk. Freezing of pore water may have been caused by either rapid cooling downward from the rock top and/or upward from the simulated permafrost, which may explain the depth distribution of AEs shown in Figures 8 and S2: F3–F5.

The timing of AE activity under laboratory conditions may be compared with that reported under field conditions. At 3500 m above sea level in the Swiss Alps, AE activity and rock temperature

444 monitored during the course of four days in a south-facing alpine rockwall formed of granitic gneiss
445 revealed that AE activity increased significantly when rock temperature was <0°C, especially at
446 locations receiving meltwater from snow (Armitrano et al., 2012). Rock at 10 cm depth warmed to
447 10°C during the day and cooled to −5°C during night, while rock at 60 cm depth remained
448 continuously between about −2° to −7°C. The increased AE activity during periods of sub-zero
449 temperature, when near-surface rock experienced refreezing, suggested that freezing-induced
450 stresses contributed to rock damage. Subsequently, AE monitoring at this location for a period of
451 one year showed that rates of AE energy detected during freezing conditions were about two
452 orders of magnitude greater than those under thawed conditions, suggesting that freezing-induced
453 processes largely accounted for AE activity (Girard et al., 2013). AE activity during freezing periods
454 ranged over temperatures from just below 0°C—which might indicate in situ freezing and
455 volumetric expansion—down to as low as −15°C—consistent with water migration and ice
456 segregation. A major difference between the field site and our laboratory experiment is rock
457 porosity: the interjoint porosity of the granitic gneiss (1–2 %) is far lower than that of the tuffeau
458 (~47%; Murton et al., 2000). Thus, it is to be expected that the intact bodies of gneiss between
459 fractures will be much less susceptible to migration of liquid water and resultant ice segregation
460 than the tuffeau. At a rock slope developed in conglomerate in Austria, some AE activity coincided
461 with freeze–thaw temperature cycles, and has been linked to observed detachment of boulders
462 from the slope (Codeglia et al., 2017).

463 ## 4.2 Depth of AE events and macrocracks

464 The depth of AE events during phases 1 to 4 of the experiment (Figure 8) shows only limited
465 correspondence to the depth of macrocracks observed after phases 2, 3 and 4 (Figure 9). In phase 1
466 the majority of AEs—both in terms of total number and high magnitude (>60 dB)—were

concentrated below 180 mm depth, peaking between 250 and 300 mm depth (Figure 8a and e). In phase 2 the modal depth decreased to ~190–260 mm (Figure 8b and f), whereas in phases 3 and 4 AEs were more uniformly distributed with depth (Figure 8c, d, g and h). Macrocrack development, by contrast, was observed to form a brecciated horizon initially at 70–110 mm depth by the end of phase 2 (Figure 9a), followed by a second, deeper brecciated horizon at 180–220 mm depth during phases 3 and 4 (Figure 9b and c). The increase in depth of brecciation during the experiment has been attributed to overall deepening of the simulated active layer above permafrost between phases 1 and 4 (Figure 1a; Maji and Murton, 2020a).

The limited correspondence between the depths of AE events and macrocracks is attributed tentatively to three factors. First, the abundant AEs recorded in the basal part of the block during phase 1 were mostly of low amplitude (40–50 dB; Figure S1) and may be explained by the low temperature protocol followed at the base. Such AEs did not lead to any observed macrocracks, possibly because many AEs resulted from volumetric expansion within the pores during freezing periods and thaw-to-freeze transitions. Second, some vertical to subvertical macrocracks developed in the chalk, indicating that macrocrack development was not confined to the two brecciated horizons but was more widely distributed in the block. Such cracks may function as conduits for migration of unfrozen water towards the freezing front to facilitate ice segregation (Fukuda, 1983; Maji and Murton, 2020a). Third, the number of AEs decreased overall during the course of the experiment (Figure 8), consistent with reduced amounts of AE activity with increasing numbers of freeze–thaw cycles reported in experiments on concrete (Todak et al., 2017) and granite (Wang et al., 2019). This progressive reduction in AE activity probably resulted, at least in part, from increasing heterogeneity in the chalk, as the macrocracks propagated. Increasing heterogeneity as the rock fractured likely caused increasing attenuation of the AE signal (cf. Weber et al., 2018), which may have limited the number of AEs registered by the sensors around the block.

4.3 Mechanisms and modes of cracking

Mechanistically, ice segregation alone may have caused microcracking during thawing periods and freeze-to-thaw transitions, but we discount volumetric expansion at such times as a cause because phase change from liquid water to ice requires rock cooling and freezing. However, both ice segregation and/or volumetric expansion may have caused microcracking during freezing periods and thaw-to-freeze transitions.

Moderate- to high-amplitude (64–80 dB) AE activity during freeze-to-thaw transitions was observed as clusters near faces A and C early in the experiment, suggesting that development of new clusters was facilitated at the face boundaries, followed by high-magnitude events (>70 dB). In phase 1 (i.e., lowest thermal boundary conditions; Figure 1a), the dominant low-magnitude tension mode of cracking suggests that the microcracks were caused by volumetric expansion mostly during freezing periods and thaw-to-freeze transitions as the chances of well-developed lenses of segregated ice were minimal in the early phases of the experiment. By contrast, AE events during thawing periods in P1 were mostly isolated near the face boundaries (Figure S10: panels 1–4), whereas in freeze-to-thaw transitions, some events occurred within the block (Figure S4: panels 1–4), which suggests that melting of ice initiated events within the well-developed clusters near the face boundaries. Also, high-amplitude events in the upper half of the block during thawing periods in P1 correlate with the well-developed brecciated layer at ~70–110 mm depth.

In P2–3, moderate- to high-amplitude events (56–72 dB) occurred within the block, implying that warmer thermal boundary conditions were suitable for developing segregated ice lenses. However, the clustering of high-magnitude activity near the faces suggests that surface boundaries are weaker zones for initiation of ice lenses than within the block due to the differences in confining pressure, as high pressure favours melting of ice even if the temperature gradient remains identical. In addition, the magnitude of shearing events increased in P2–3, which is

interpreted to indicate the coalescence of microcracks into developing macrocracks. Specifically, ice segregation was facilitated as the basal temperature conditions increased and the time duration was enhanced in P2–3 than in P1 and corresponds with crack coalescence by connecting isolated clusters developed in P1, as evident by the well-developed brecciated layers at depths from ~100 mm to ~200 mm.

In thawing periods, the tension activity was most abundant within the 30–40 kHz window (Figure S13–S14) compared to freeze-to-thaw transitions, where <30 kHz events were also recorded (Figure S7–S8). During thawing periods the temperature gradient allows for the development of segregated ice within the pre-existing cracks and voids that open up the cracks in tension mode. Depending on the size of the segregated ice lenses, the magnitude of tension events varied and in the case of thawing comparatively higher magnitude activity was recorded. In contrast, freeze-to-thaw transitions recorded higher magnitude shear events than thawing periods (Figures S8 and S14). We hypothesize that in freeze-to-thaw transitions, partial melting of ice crystals formed during freezing periods begins and the premelting layer of water acts as a slip surface for fracture to slide one after another, causing relatively high-magnitude shearing activity observed in freeze-to-thaw transitions.

4.4 Statistical modelling of crack propagation

Maji and Murton (2020b) classified different zones of microcracking based on micro-computed tomography (μ-CT) analysis of 20 freeze–thaw cycles of a cylindrical core of the same chalk lithology (30 mm long, 20 mm diameter). However, the mechanisms of crack propagation were not identified. For the statistical model of crack propagation proposed in the present study, the results of the hypothetical simulation were compared with the experimental results. The relationships between the proposed mechanisms of crack propagation (inside–out and outside–in) and the

538 modes of cracking (tension, shear and mixed) are summarised in a Venn diagram (Figure 14). It is
539 evident that each mode of propagation consists of cracks of tension, shear and mixed modes of
540 origin.

541 Probabilistic assessment of the experimental results based on Bayes' theorem is summarised in
542 Table 5 for the four parts of each freeze–thaw cycle (freezing period, freeze-to-thaw transition,
543 thawing period and thaw-to-freeze transition). For each part, the probability of occurrences of any
544 particular type of event was assessed based on prior knowledge related to the prevalence of that
545 event. Column two represents the probability of occurrences of tension events provided that the
546 inside-out mode of propagation had occurred as a related background condition. The reverse
547 scenario is represented in column three, where the probability of the inside-out mode of
548 propagation is evaluated following the prior correlated condition assuming that the tension mode
549 of cracking had taken place. Column four illustrates the probability of occurrences of shearing
550 events following the condition that the outside-in mode of propagation has occurred. Column five
551 documents the opposite situation, evaluating the probability of outside-in events when shearing
552 modes of cracking existed. Overall, we tested the hypothesis that the inside–out mode of crack
553 propagation (i.e., increasing $\mathbb{FP}$) is facilitated by tensional cracks, whereas the outside–in mode is
554 assisted by shearing cracks (i.e., decreasing $\mathbb{FP}$). The hypothesis is supported by 54% (minimum) to
555 73% (maximum) confidence level, with an average of 64.88% for various parts of freeze–thaw
556 cycles.

557 Acceptance of the hypothesis suggests that the inside-out and outside-in approach of
558 quantifying the fracture propagation method—based on statistical modelling of the crack
559 propagation dynamics—was influenced to some extent by the modes of cracking (tension, shearing,
560 and mixed). By implication, the growth of any crack that develops under such dynamic thermal
561 boundary conditions can be broadly predicted.

4.5 Application of crack propagation model for isolating volumetric expansion and ice segregation mechanisms

The negative trends for both $\mathbb{FP}$ (r) and $\mathbb{FP}$ (θ) were relatively steep in P1 compared to other phases, and contained short episodes of increase (Figures 10–13). Some episodes of tensional activity attributed to volumetric expansion formed at various locations throughout the depth window, and started to interact with each other, as indicated by the sharp decreases in $\mathbb{FP}$ (r) and $\mathbb{FP}$ (θ). In P2, when the thermal protocol was higher than P1, the slope of the negative trend reduced, and the episodic spikes in positive trend increased. The increases were of steep slope, suggesting potential tensional events attributed to ice segregation that may have allowed growth of thicker ice lenses as compared to volumetric expansion when an extreme thermal protocol was established. Similar mechanisms were inferred during P3 as well when the temperature protocols were identical with that of P2 except some high-magnitude spikes. Similar repeated spikes occurred in P4, when the temperature at the bottom of the block was highest. Such spikes were correlated with the hypothesized thicker ice lenses as thermal protocols and duration of freezing and thawing cycles were highest, favouring ice segregation. This also correlated with the brecciated horizon at ~70–110 mm depth that was partially formed after 8 FT cycles but well developed after 16 cycles.

4.6 Limitations and recommendations for future research

The present study investigated the applicability of using AEs as a non-destructive method during rock freezing and thawing for an order of magnitude longer duration than previous experiments (Hallet et al., 1991; Duca et al., 2014) and, for the first time, during dynamic thermal conditions. However, some limitations of our experiment are apparent.

First, the dynamic thermal boundary conditions around the chalk block imposed a vertical thermal gradient, causing the lower part to remain frozen during most of the experiment, while the upper part experienced repeated freeze–thaw. We assumed a uniform AE wave velocity

throughout for detecting the 3D locations of the micro- and macrocracking events, although the variation in temperature changes the consistent attenuation of the AE wave velocities.

Second, deformation-induced heterogeneity was excluded in the present study. However, it was observed that the degree of deformation controls the waveform attenuation to a certain extent. The intact specimen at the beginning of the experiment showed a steady value of attenuation and the wave velocity may have varied through time as the material developed brecciated horizons and other macrocracks.

In view of both limitations, we therefore recommend that future experiments consider the temperature- and deformation-induced changes in AE wave velocities for precisely locating the cracking events in 3D as these two factors influence the attenuation of AE waveforms.

5. Conclusions

The following conclusions are drawn from the present study:

1. AE events occurred mostly during thawing periods (45%) and freeze-to-thaw transitions (37%) rather than during freezing periods (9%) and thaw-to-freeze transitions (8%). This observation supports the hypothesis that the majority of AE activity was associated with rock fracture caused by ice segregation rather than volumetric expansion.
2. The modal depths of AE events were poorly correlated with the depths of macrocracks that comprised two brecciated horizons. Possibly, the low-magnitude AE events have limited influence on developing the brecciated horizons.
3. Early phases of the experiment revealed significant AE activity around the vertical faces of the block, whereas later phases had high-magnitude events within it. This suggests that face boundaries are weaker regions where microcracking initiated, compared to interior regions. We

hypothesize that lower confining pressure around the faces facilitates stable growth of ice crystals.

4. Phase one of the experiment—with lowest basal temperature protocol (−15°C)—was dominated by tension mode microcracking, which suggests that the lowest temperatures initiated volumetric expansion. Higher basal temperature protocols in phases 2 (−10°C) and 3 (−5°C) were associated with shearing events, allowing stable growth of ice lenses developed mainly by ice segregation. The magnitude of tension mode cracking was higher during thawing periods, facilitating development of ice lenses. By contrast, the occurrence of high-magnitude shearing events mostly during freeze-to-thaw transitions is hypothesized to indicate that partial melting of ice provided slip surfaces (of low friction) for fractures to slide over the thin film of premelted water.
5. Microcrack propagation from inside the block towards the outside (inside-out mode) favoured tensional cracking, whereas propagation from the outer part of the block towards the interior (outside-in mode) favoured shearing events.
6. The proposed microcrack propagation model can distinguish reasonably between cracks formed by volumetric expansion and ice segregation, based on the slope of the probabilistic values connecting the distance and angular relationships of corresponding events.

Acknowledgements

This research is part of the senior author's doctoral research at the University of Sussex. The research was funded by a Chancellor's international research scholarship and a Global Studies studentship in the Department of Geography. Tim Cane provided help and guidance with experimental design, sample preparation and use of equipment in the Permafrost Laboratory. Rhys Pullin and Matthew Pearson (Institute of Mechanical and Manufacturing Engineering, Cardiff

University) provided guidance about acoustic emissions and access to rock testing apparatus. Marcus Dodds, Ed Haslam and Russell Swift (British Geological Survey, Keyworth) provided advice about acoustic emissions. Peter Cleall (Cardiff University) and John Barlow (University of Sussex) are thanked for comments on an earlier version of the manuscript.

Data availability statement

The dataset for this research is available from the University of Sussex Research Data Repository https://doi.org/10.25377/sussex.14040029

Private link for review purposes: https://figshare.com/s/84dc99c3ed21a9e8597e

References

Akagawa, S., & Fukuda, M. (1991). Frost heave mechanism in welded tuff. *Permafrost and Periglacial Processes*, *2*(4), 301–309. https://doi.org/10.1002/ppp.3430020405

Armitrano, D., Gruber, S., & Girard, L. (2012). Evidence of frost-cracking inferred from acoustic emissions in a high-alpine rock-wall. *Earth and Planetary Science Letters, 341–344*, 86–93. https://doi.org/10.1016/j.epsl.2012.06.014

Azmatch, T. F., Arenson, L. U., & Sego, D. C. (2008). Measuring ice lens growth and development of soil strains during frost penetration using particle image velocimetry (GeoPIV). In Kane DL, Hinkel KM. (Eds.), *Proceedings of the 9th International Permafrost Conference, 29 June–3 July 2008, University of Alaska Fairbanks.* (Vol. 1, pp. 89–93). Fairbanks: Institute of Northern Engineering, University of Alaska Fairbanks.

Ballantyne, C. K. (2018). *Periglacial Geomorphology*. Chichester: Wiley.

Codeglia, D., Dixon, N., Fowmes, G. J., & Marcato, G. (2017). Analysis of acoustic emission patterns for monitoring of rock slope deformation mechanisms. *Engineering Geology, 219*, 21–31. https://doi.org/10.1016/j.enggeo.2016.11.021

654 Dash, J. G., Rempel, A. W., & Wettlaufer, J. S. (2006). The physics of premelted ice and its
655 geophysical consequences. *Reviews of Modern Physics, 78*(3), 695–741.
656 https://doi.org/10.1103/RevModPhys.78.695
657 Duca, S., Occhiena, C., Mattone, M., Sambuelli, L., & Scavia, C. (2014). Feasibility of ice segregation
658 location by acoustic emission detection: a laboratory test in gneiss. *Permafrost and Periglacial*
659 *Processes, 25*(3), 208–219. https://doi.org/10.1002/ppp.1814
660 Fukuda, M. (1983). The pore water pressure in porous rocks during freezing. In *Proceedings of the*
661 *Fourth International Conference on Permafrost, 17-22 July, Fairbanks, Alaska*. (pp. 322–337).
662 Washington, DC: National Academy of Sciences.
663 Girard, L., Gruber, S., Weber, S., & Beutel, J. (2013). Environmental controls of frost cracking
664 revealed through in situ acoustic emission measurements in steep bedrock. *Geophysical*
665 *Research Lett*ers, *40*(9), 1748–1753. https://doi.org/10.1002/grl.50384
666 Goszczyńska, B. (2014). Analysis of the process of crack initiation and evolution in concrete with
667 acoustic emission testing. *Archives of Civil and Mechanical Engineering*, *14*(1), 134–143.
668 https://doi.org/10.1016/j.acme.2013.06.002
669 Hall K. (1999). The role of thermal stress fatigue in the breakdown of rock in cold regions.
670 *Geomorphology, 31*(1–4), 47–63. https://doi.org/10.1016/S0169-555X(99)00072-0
671 Hallet, B., Walder, J. S., & Stubbs, C. W. (1991). Weathering by segregation ice growth in
672 microcracks at sustained sub-zero temperatures: verification from an experimental study using
673 acoustic emissions. *Permafrost and Periglacial Processes, 2*(4), 283–300.
674 https://doi.org/10.1002/ppp.3430020404
675 JCMS-IIIB5706, 2003. Monitoring method for active cracks in concrete by acoustic emission. Construction
676 Materials Standard, Federation of Construction Materials Industries, Japan, pp.23–28.

677 Jia, H., Xiang, W., & Krautblatter, M. (2015). Quantifying rock fatigue and decreasing compressive
678 and tensile strength after repeated freeze-thaw cycles. *Permafrost and Periglacial Processes,*
679 *26*(4), 368–377. https://doi.org/10.1002/ppp.1857
680 Mackay, J.R. (1974). Reticulate ice veins in permafrost, northern Canada. *Canadian Geotechnical*
681 *Journal, 11*(2), 230–237.https://doi.org/10.1139/t74-019
682 Matsuoka, N., & Murton, J. B. (2008). Frost weathering: recent advances and future directions.
683 *Permafrost and Periglacial Processes*, *19*(2), 195–210. https://doi.org/10.1002/ppp.620
684 Maji V. (2018). *An experimental investigation of micro- and macrocracking mechanisms in rocks by*
685 *freeze–thaw cycling*. (Doctoral dissertation). Brighton: University of Sussex;
686 2018.http://sro.sussex.ac.uk/79661/
687 Maji, V., & Murton, J. B. (2020a). Experimental observations that active-layer deepening drives
688 deeper rock fracture. *Permafrost and Periglacial Processes*, *31*(2), 296–310.
689 https://doi.org/10.1002/ppp.2041
690 Maji, V., & Murton, J. B. (2020b). Micro-computed tomography imaging and probabilistic modelling
691 of rock fracture by freeze–thaw. *Earth Surface Processes and Landforms, 45*(3), 666–680.
692 https://doi.org/10.1002/esp.4764
693 Michlmayr, G., Cohen, D., & Or, D. (2012). Sources and characteristics of acoustic emissions from
694 mechanically stressed geologic granular media—A review. *Earth-Science Reviews*, *112*(3–4), 97–
695 114. https://doi.org/10.1016/j.earscirev.2012.02.009
696 Murton, J. B. (2018). Frost weathering of chalk. In Lawrence JA, Preene M, Lawrence UL, Buckley R.
697 (Eds.), *Engineering in Chalk: Proceedings of the Chalk 2018 Conference, 17–18 September 2018,*
698 *Imperial College, London*. (pp. 497–502). London: ICE Publishing.

699 Murton, J. B., Peterson, R., & Ozouf, J. C. (2006). Bedrock fracture by ice segregation in cold regions.
700 *Science, 314*(5802), 1127–1129. DOI: 10.1126/science.1132127

701 Murton, J. B., Coutard, J. P., Lautridou, J. P., Ozouf, J. C., Robinson, D. A., Williams, R. B. G.,
702 Guillemet, G., & Simmons, P. (2000). Experimental design for a pilot study on bedrock
703 weathering near the permafrost table. *Earth Surface Processes and Landforms, 25*(12):1281–
704 1294. https://doi.org/10.1002/1096-9837(200011)25:12<1281::AID-ESP137>3.0.CO;2-U

705 Murton, J. B., Coutard, J. P., Ozouf, J. C., Lautridou, J.P., Robinson, D. A., & Williams, R. B. G. (2001).
706 Physical modelling of bedrock brecciation by ice segregation in permafrost. *Permafrost and*
707 *Periglacial Processes, 12*(3), 255–266. https://doi.org/10.1002/ppp.390

708 Murton, J. B., Ozouf, J. C., & Peterson, R. (2016). Heave, settlement and fracture of chalk during
709 temperature cycling above and below 0°C. *Geomorphology,* 270, 71–87.
710 https://doi.org/10.1016/j.geomorph.2016.07.016

711 Ohno, K., & Ohtsu, M. (2010). Crack classification in concrete based on acoustic emission.
712 *Construction and Building Materials*, 24, 2339–2346.
713 https://doi:10.1016/j.conbuildmat.2010.05.004

714 Rempel, A. W. (2011). Microscopic and environmental controls on the spacing and thickness of
715 segregated ice lenses. *Quaternary Research 75*(2), 316–324.
716 https://doi.org/10.1016/j.yqres.2010.07.005

717 Taber, S. (1930). The mechanics of frost heaving. *Journal of Geology, 38*(4), 303–317.
718 https://www.jstor.org/stable/30058950

719 Todak, H. N., Tsui, M., Ley, M. T., & Weiss, W. J. (2017). Evaluating freeze-thaw damage in concrete
720 with acoustic emissions and ultrasonics. In Shen, G. Wu, Z., and Zhang, J. (eds), *Advances in*
721 *Acoustic Emission Technology*. (Springer Proceedings in Physics 179, pp. 175–189). Switzerland:
722 Springer.

723 Walder, J. S., & Hallet, B. (1985). A theoretical model of the fracture of rock during freezing.
724 *Geological Society of America Bulletin*, *96*(3), 336–346. https://doi.org/10.1130/0016-
725 7606(1985)96<336:ATMOTF>2.0.CO;2
726 Walder, J. S., & Hallet, B. (1986). The physical basis of frost weathering: Toward a more
727 fundamental and unified perspective. *Arctic and Alpine Research, 18*(1), 27–32. DOI:
728 10.1080/00040851.1986.12004060
729 Wang, Y., Feng, W., Wang, H., Han, J., & Li, C. (2019). Geomechanical and acoustic properties of
730 intact granite subjected to freeze–thaw cycles during water-ice phase transformation in
731 Beizhan's Open Pit Mine Slope, Xinjiang, China. *Water, 11*(11), 2309.
732 https://doi.org/10.3390/w11112309
733 Weber, S., Faillettaz, J., Meyer, M.,Beutel, J., & Vieli, A. (2018). Acoustic and microseismic
734 characterization in steep bedrock permafrost on Matterhorn (CH). *Journal of Geophysical*
735 *Research: Earth Surface*, *123*(6), 1363–1385. https://doi.org/10.1029/2018JF004615

736
737

Tables

Table 1. Number and magnitude of AE events occurred during freezing periods.

Cycles	Number of AE events	Amplitude (dB)					
		>40 & < 49	>49 & < 57	>57 & < 65	>65 & 73	>73 & <81	>81
F3	231	142	69	16	4	0	0
F4	751	506	176	55	14	0	0
F5	873	604	198	55	12	4	0
F10	43	23	9	10	1	0	0

Table 2. Number and magnitude of AE events occurred during freeze-to-thaw transitions.

Cycles	Number of AE events	Amplitude (dB)					
		>40 & <49	>49 & <57	>57 & <65	>65 & <73	73 & < 81	>81
FT1	1792	900	506	313	70	3	0
FT 2	448	159	148	98	33	10	0
FT 3	734	434	246	52	2	0	0
FT 4	195	129	47	18	1	0	0
FT 5	180	72	86	21	1	0	0
FT 6	533	335	121	62	14	1	0
FT 7	334	187	90	43	13	1	0
FT 8	119	88	23	4	4	0	0
FT 9	361	171	93	67	23	4	3
FT 10	252	110	79	38	22	3	0
FT 11	487	230	155	78	21	3	0
FT 12	476	280	140	44	11	1	0
FT 13	582	297	186	73	24	2	0
FT 14	520	386	108	23	3	0	0
FT 15	392	190	147	45	10	0	0
FT 16	11	7	4	0	0	0	0

746 **Table 3**. Number and magnitude of AE events occurred during thawing periods.

Cycles	Number of AE events	Amplitude (dB)					
		>40 & < 49	>49 & <57	>57 & < 65	>65 & < 73	>73 & < 81	>81
T1	4	2	1	1	0	0	0
T2	368	188	143	34	3	0	0
T3	647	393	206	48	0	0	0
T4	369	235	102	30	2	0	0
T5	395	211	157	26	1	0	0
T6	685	372	255	56	2	0	0
T7	4219	2488	1526	183	20	2	0
T8	730	46	252	432	0	0	0
T10	497	277	153	62	5	0	0
T11	585	307	206	60	12	0	0
T12	156	69	54	33	0	0	0
T13	294	148	124	22	0	0	0
T14	150	72	74	4	0	0	0
T16	5	5	0	0	0	0	0

747

748 **Table 4**. Number and magnitude of AE events during thaw-to-freeze transitions.

Cycles	Number of AE events	Amplitude (dB)					
		>40 & <49	>49 & < 57	>57 & < 65	>65 & <73	>73 & <81	>81
TF2	543	311	178	37	16	1	0
TF 3	255	177	66	12	0	0	0
TF 4	286	210	57	19	0	0	0
TF 5	222	144	65	12	1	0	0
TF 7	290	197	77	13	3	0	0
TF 8	11	0	0	11	0	0	0
TF 9	9	4	4	0	1	0	0
TF 13	8	3	4	1	0	0	0
TF 14	2	1	1	0	0	0	0
TF 15	14	12	1	1	0	0	0

749

750

751

752 **Table 5**. Summary of probability (P) values based on Bayes' theorem for testing the hypothesis that
753 inside–out (IO) mode of crack propagation is supported by tensional activity (T), whereas the
754 outside–in (OI) mode is supported by shearing activity (S).

Part of freeze–thaw cycle	P(T|IO)	P(IO|T)	P(S|OI)	P(OI|S)
Freeze	0.57	0.68	0.73	0.67
Freeze-to-thaw	0.63	0.63	0.58	0.61
Thaw	0.73	0.66	0.54	0.69
Thaw-to-freeze	0.66	0.67	0.61	0.72

755

756

Figures

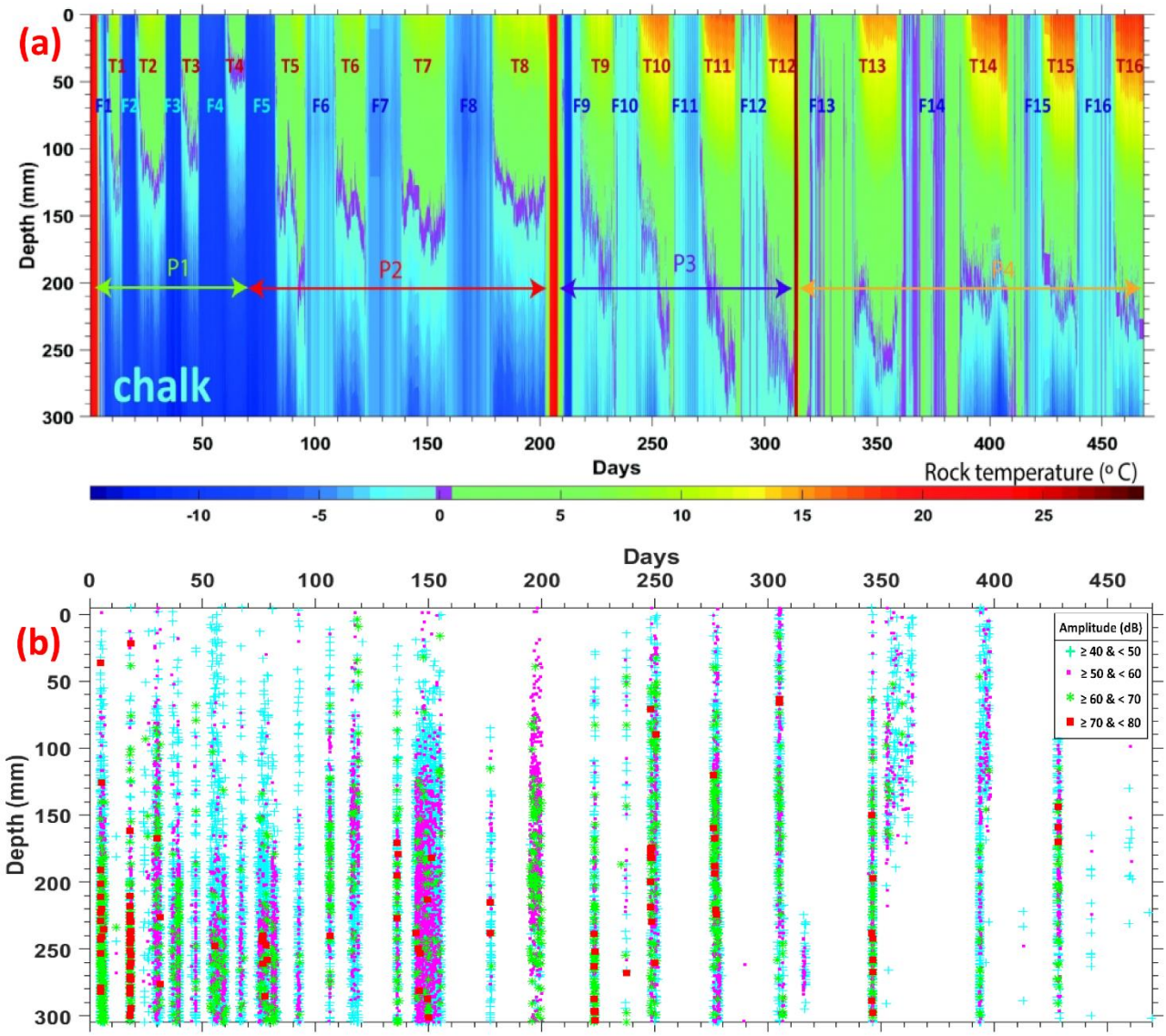

Figure 1. (a) Time series of vertical temperature profile (a) and amplitude of acoustic emission (AE) events (b) in the chalk block during the 16 freeze–thaw cycles, divided into phases 1 to 4 (P1–P4). F1 to F16 denote freezing periods, and T1 to T16 denote thawing periods.

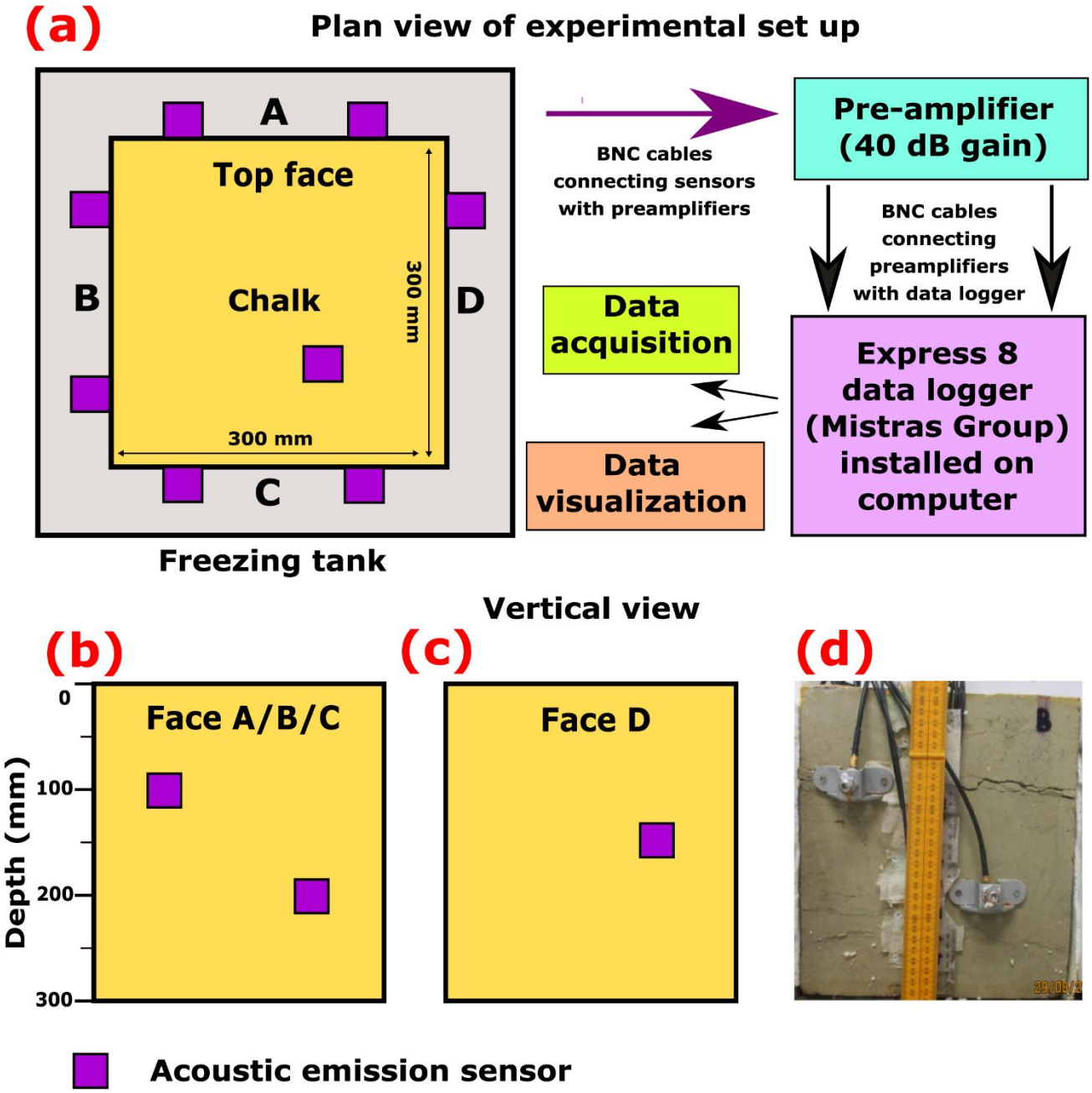

764

765 **Figure 2**. Diagrams showing locations of eight AE sensors on the chalk block. (a) Plan view of the top
766 face with layout of the experimental set up, illustrating the hardware interfaces. (b) Vertical view of
767 three faces A, B and C, each hosting two AE sensors along the diagonal. (c) Vertical view of face D,
768 with one AE sensor. (d) Photograph showing two AE sensors mounted on face B within metal cages
769 attached to the chalk block. Note well-developed brecciated horizon at ~100 mm depth and
770 incipient fractures at ~200 mm depth after 12 freeze–thaw cycles.

771

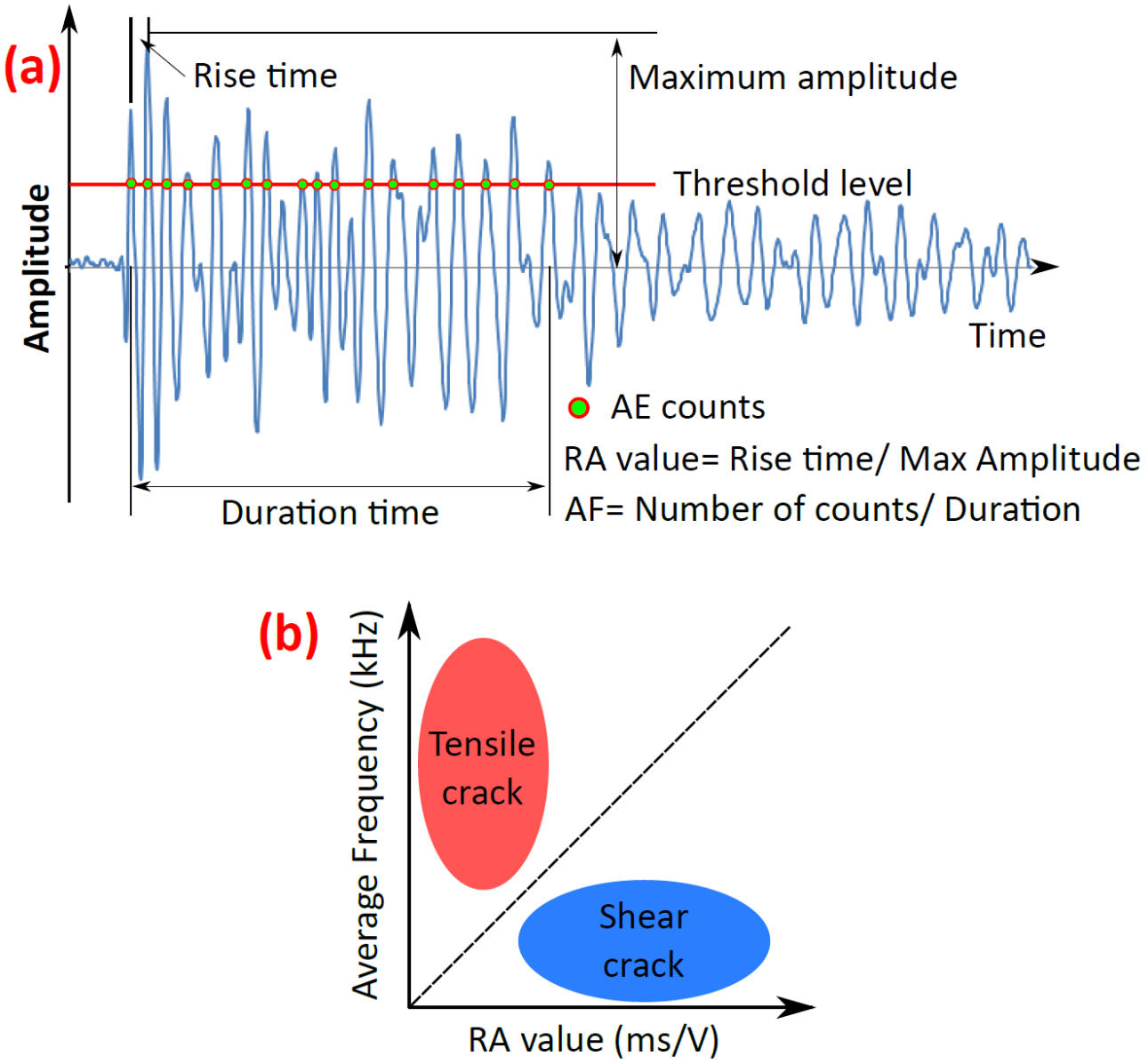

772
773 **Figure 3**. Schematic diagrams of (a) different waveform parameters of the acoustic waves, (b) RA vs
774 average frequency plot to discriminate tension and shear fracture. Source: modified from Ohno et
775 al., 2010.
776

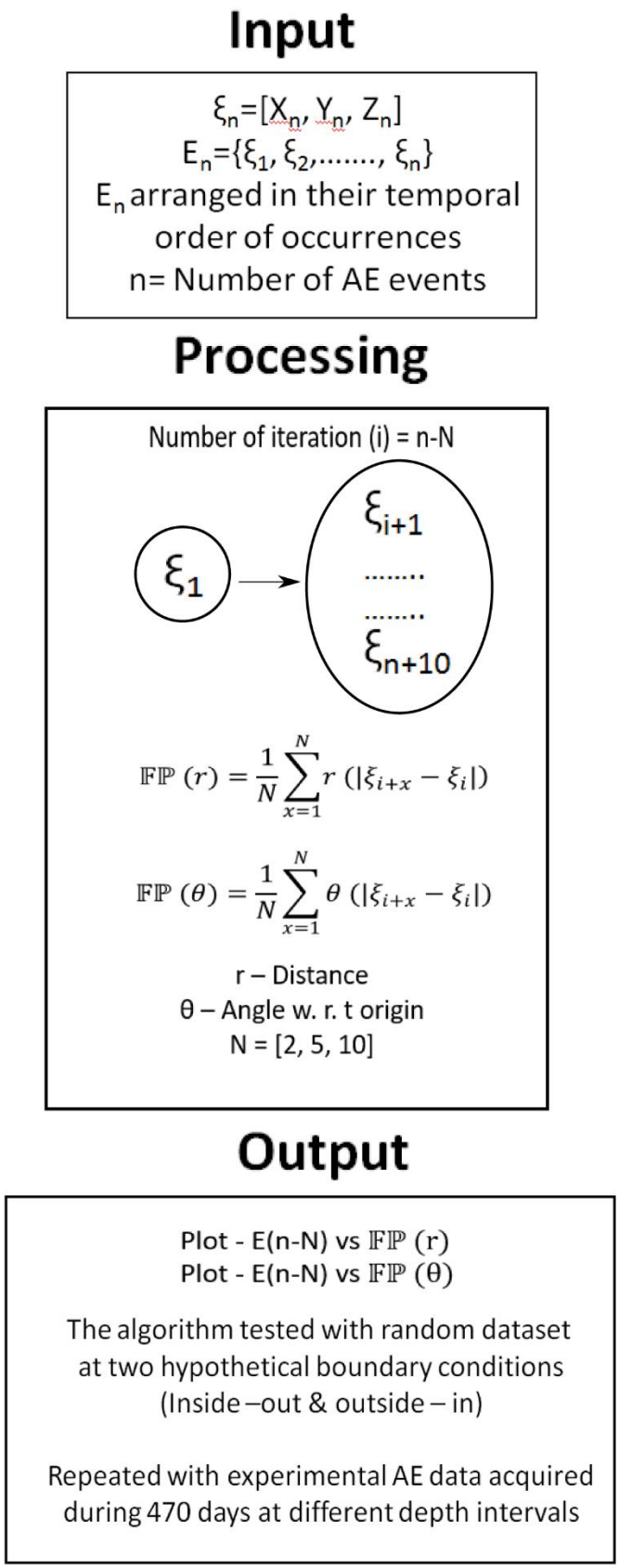

Figure 4. Schematic diagram explaining the input of 3-D AE locations following their temporal occurrence, subsequent processing and final output of crack propagation hypothesis.

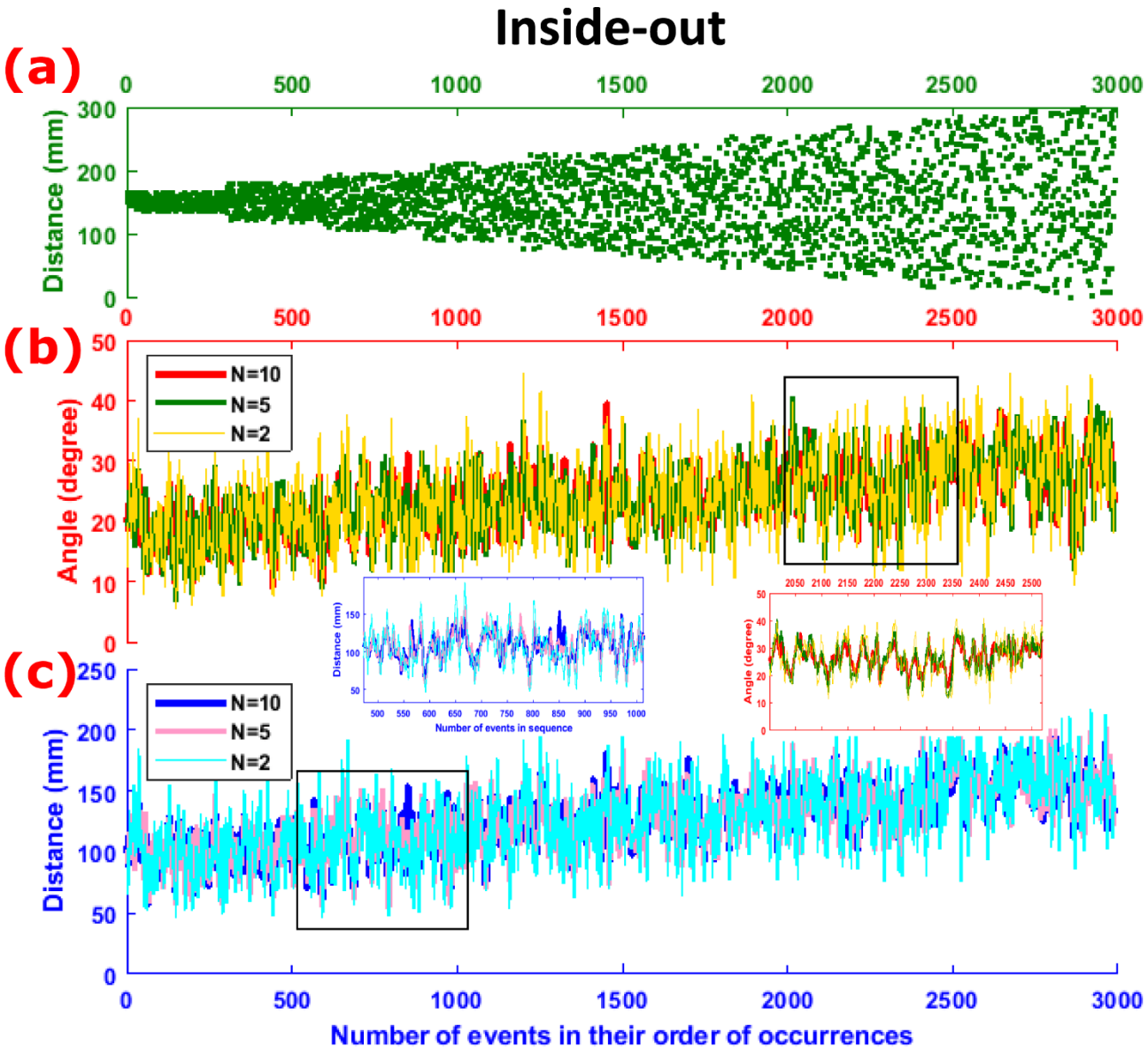

781
782 **Figure 5**. The inside–out model of fracture propagation. (a) Locations of the random points along Y-
783 direction. (b) Angular relationships with varying number (N=2, 5, 10) of next consecutive events. (c)
784 Distance relationships with N=2, 5 and 10 of next consecutive events. Inset figures show enlarged
785 views of specific portions of the angular and distance variations marked by rectangular boxes.
786

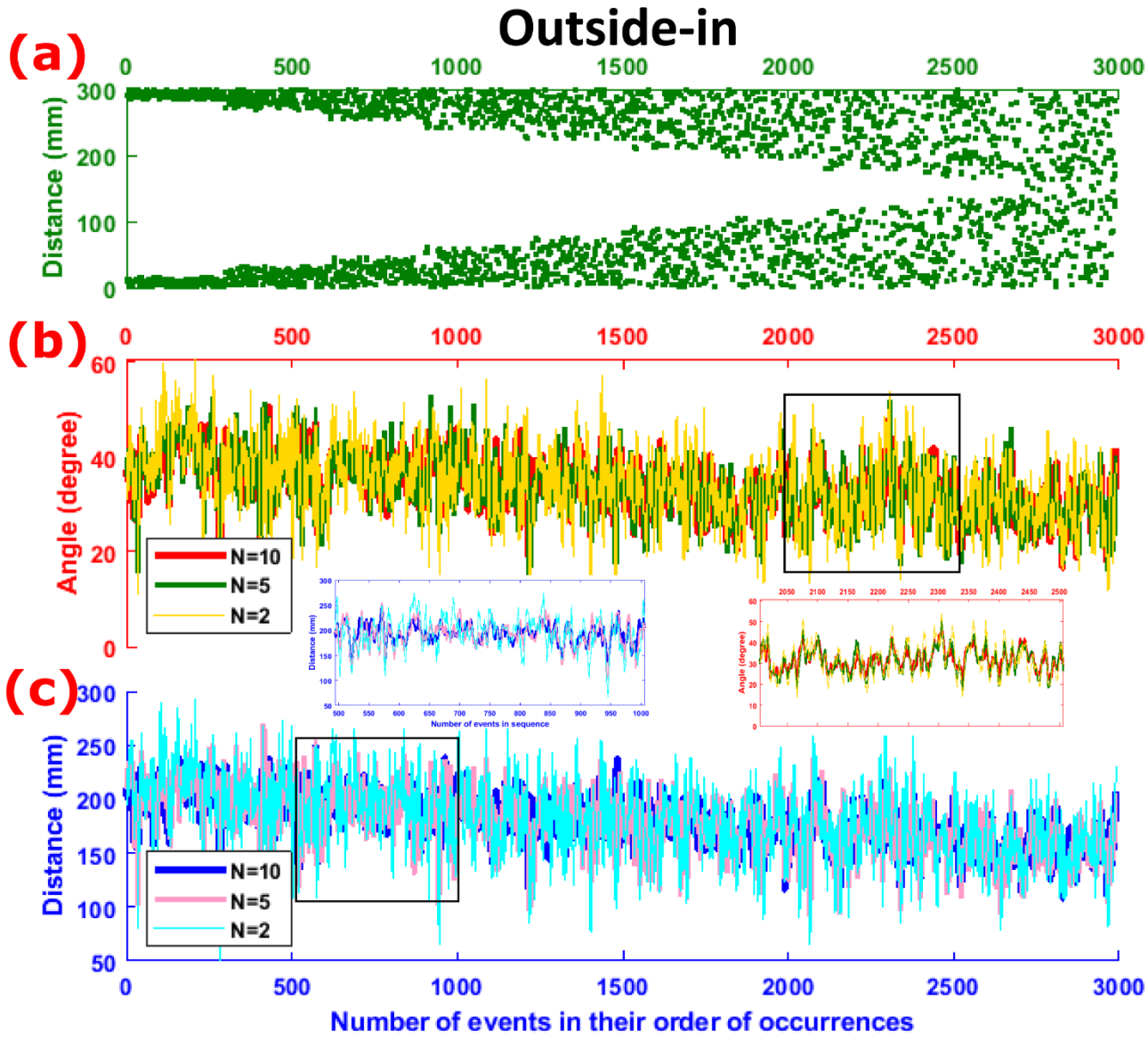

Figure 6. The outside–in model of fracture propagation. (a) Locations of the random points along Y-direction. (b) Angular relationships with varying number (N=2, 5, 10) of next consecutive events. (c) Distance relationships with N=2, 5, 10 of next consecutive events. Inset figures show enlarged views of specific portions of the angular and distance variations marked by rectangular boxes.

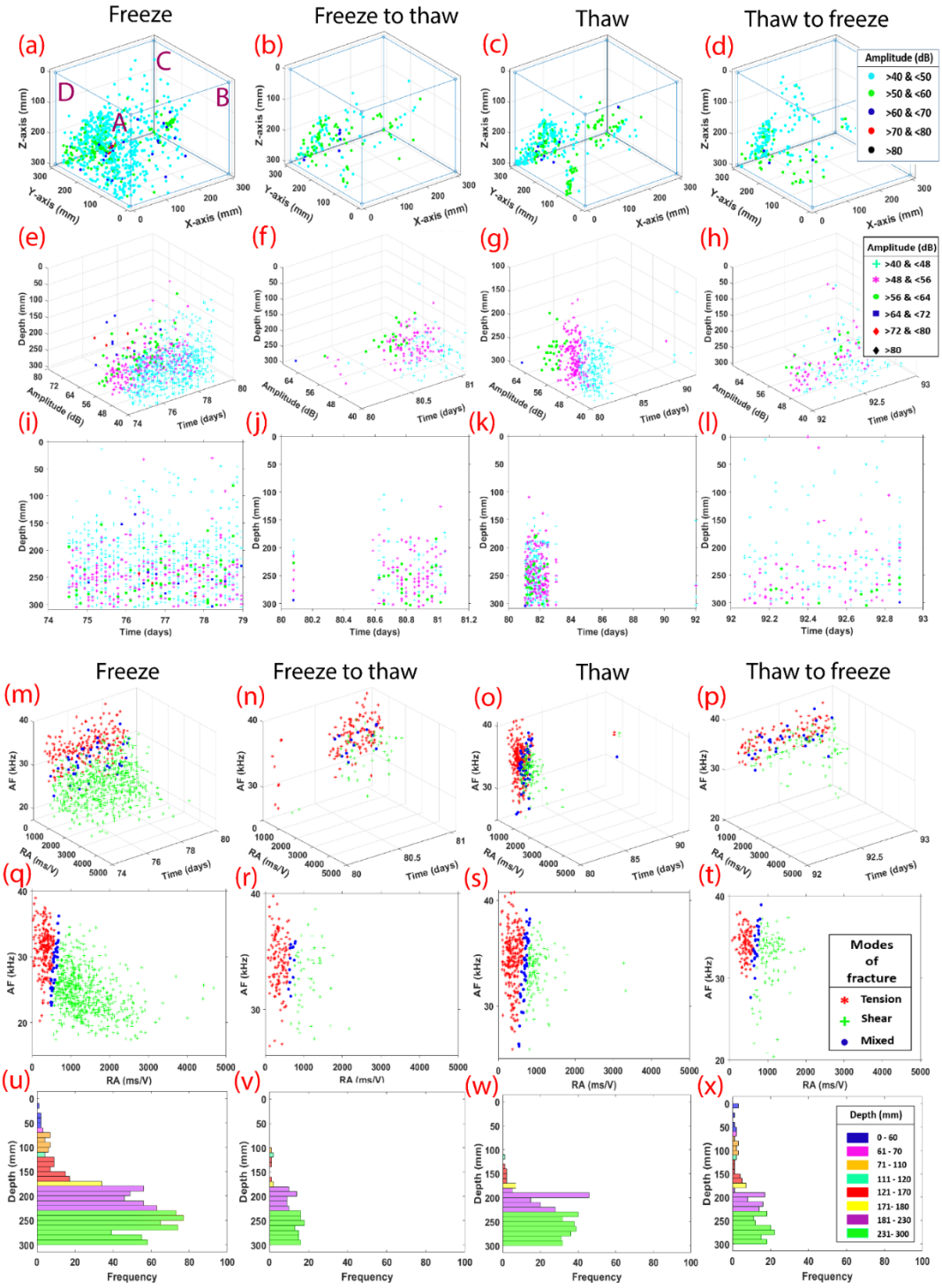

Figure 7. AE data for freeze–thaw cycle 5 divided into four constituent parts: freezing period ('freeze'), freeze-to-thaw transition, thawing period ('thaw') and thaw-to-freeze transition. (a–d) 3D locations of AE events with their respective amplitude. Vertical faces A–D of the block are labelled in (a); this labelling applies to all subsequent 3D plots in the article. (e–h) Visualization of AE events in terms of depth, amplitude and time. (i–l) Simplified version of plots e–h with depth vs time, and amplitude ranges marked with different shapes and colours. (m–p) Visualization of AE events in terms of AF values, RA values and time, labelled according to modes of fracture. (q–t) Simplified version of plots m–p with AF vs RA values and fracture modes. (u–x) Frequency distribution of AE events along various depth intervals within the block.

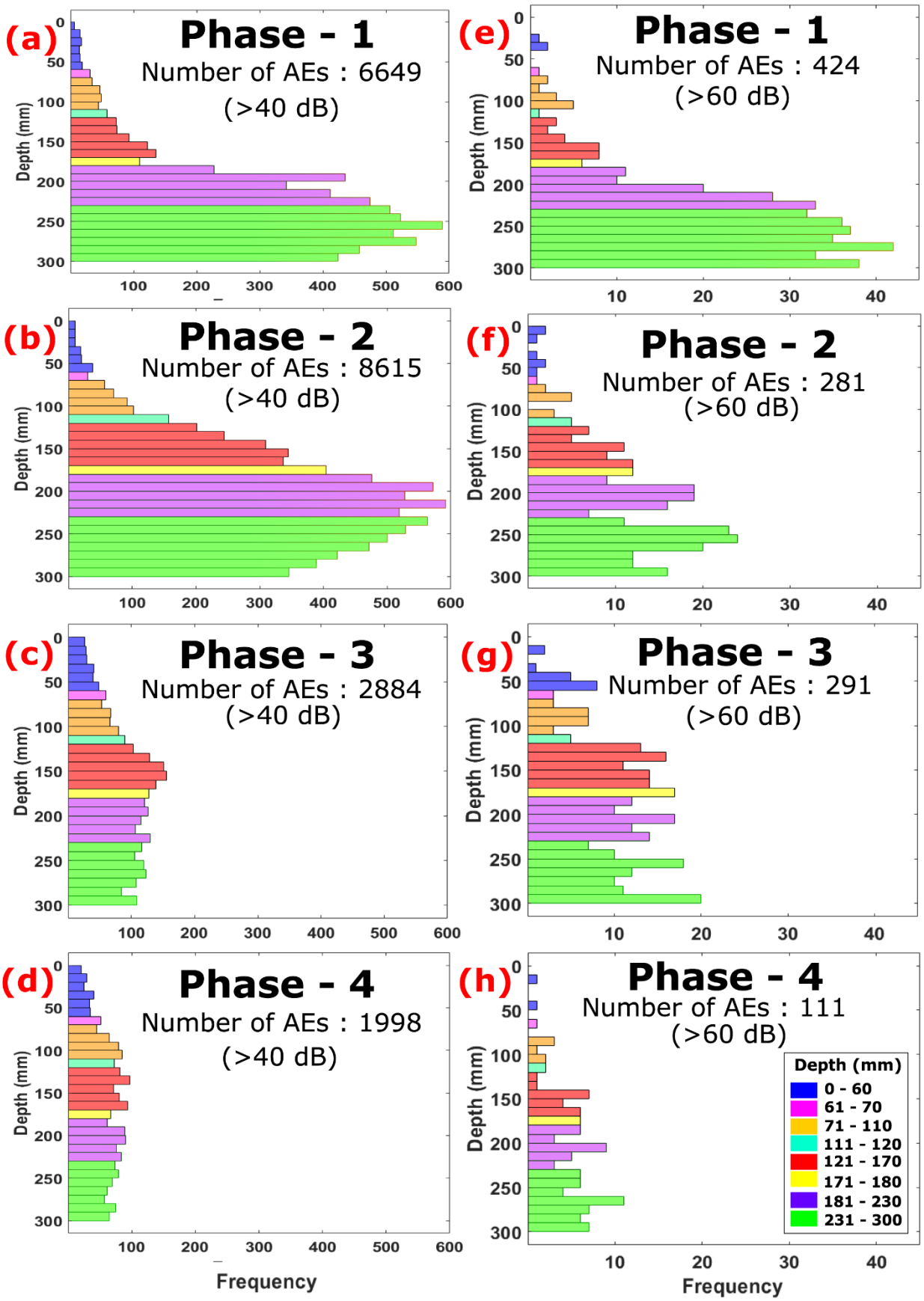

Figure 8. Acoustic emission (AE) frequency versus depth during phases 1 to 4 of the experiment. (a–d) All AEs (>40dB), (e–h) AEs of higher magnitude (>60 dB).

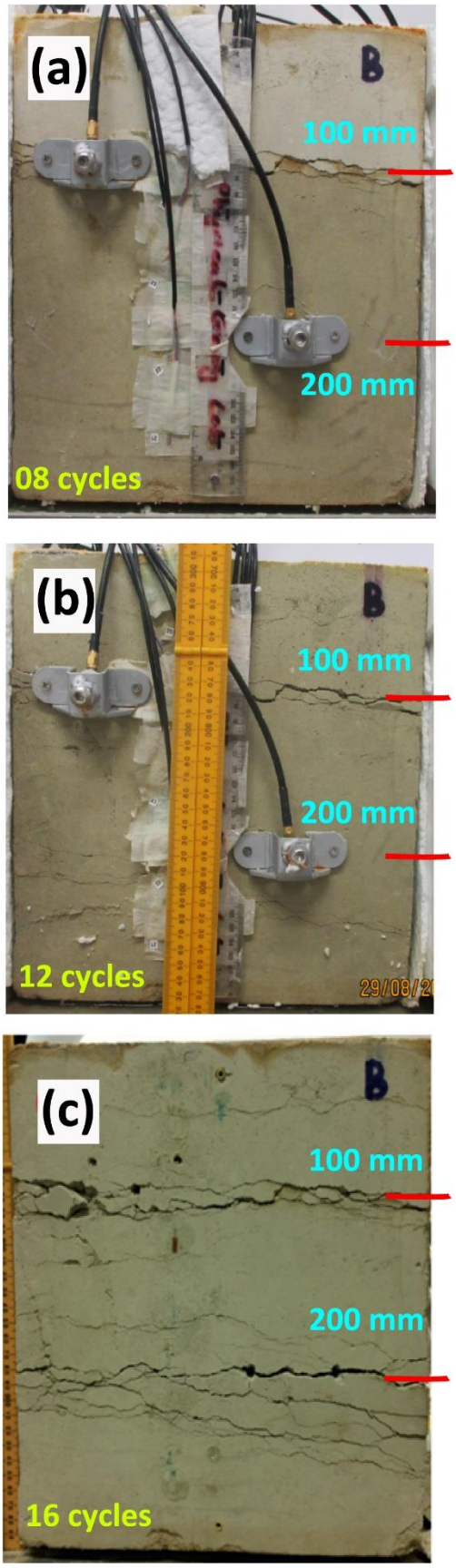

Figure 9. Photographs of macrocracks and brecciated horizons in vertical face B of the chalk block after 8, 12 and 16 freeze–thaw cycles (a–c, respectively). Depth intervals used for the analysis of the crack propagation models are marked.

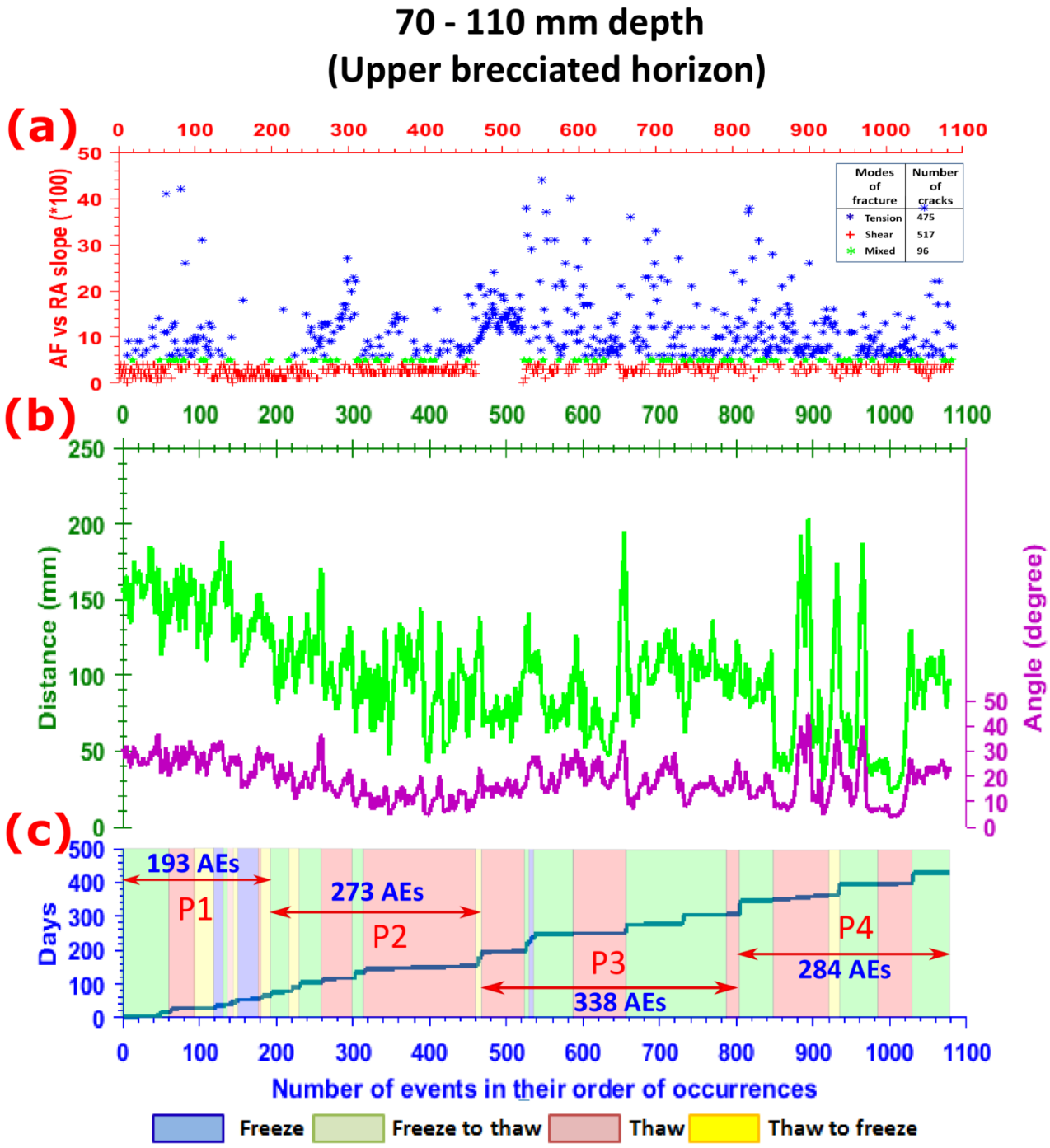

Figure 10. AE events within the 70–120 mm depth interval arranged in their order of occurrence during the four phases (P1–4) of the experiment. (a) AE events classified as tension, shear and mixed modes of cracking based on the parametric analysis of AE waveforms, using AF vs RA values. (b) $\mathbb{FP}$ (r) and $\mathbb{FP}$ (θ) values indicated on Y-axes on left and right, respectively, of the corresponding events. (c) Timing of AE events during P1–4 and subdivided into the four constituent parts of the freeze–thaw cycles (freeze, freeze-to-thaw transition, thaw, and thaw-to-freeze transitions).

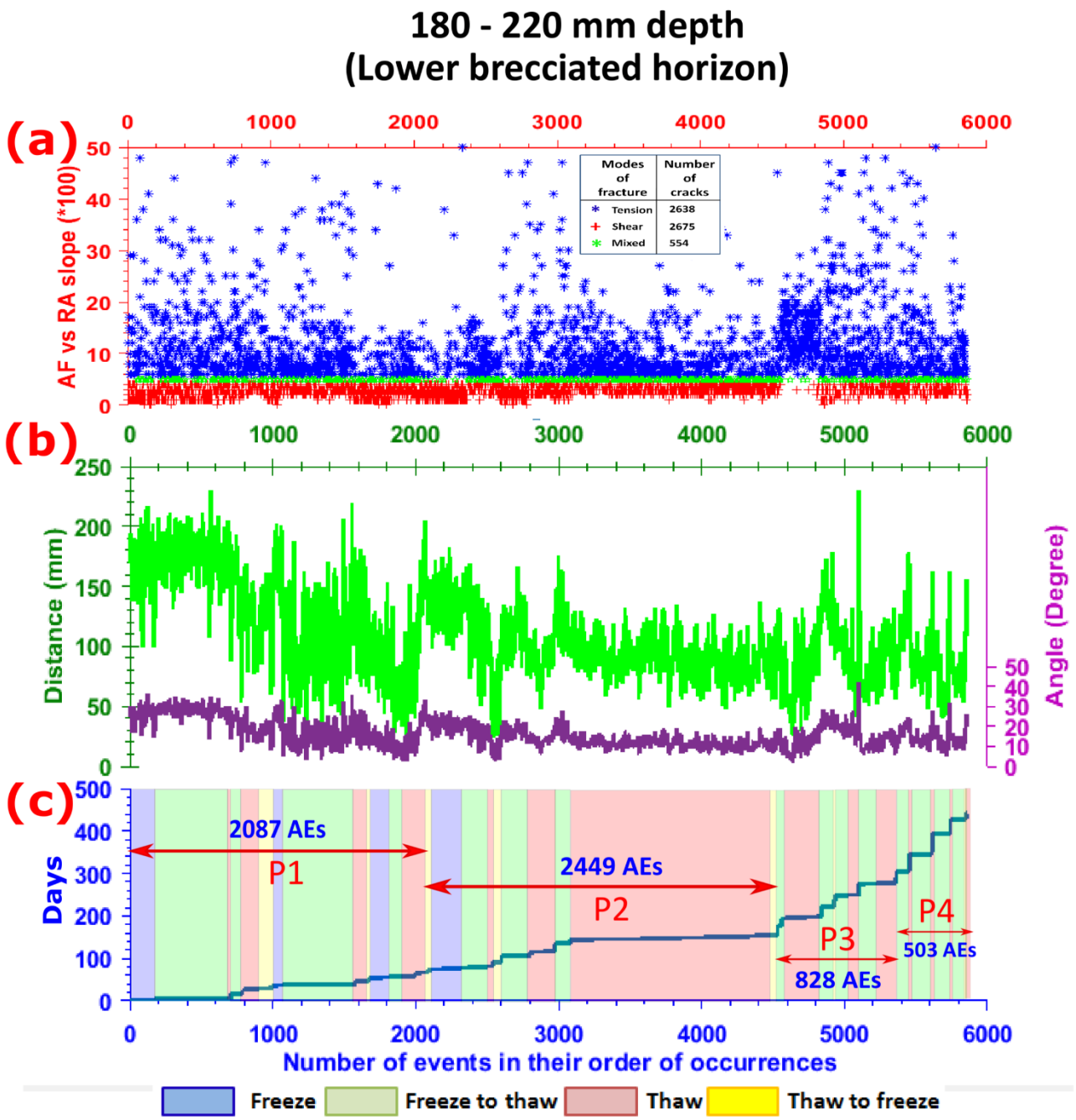

Figure 11. AE events within the 180–220 mm depth interval arranged in their order of occurrence during the four phases (P1–4) of the experiment. (a) AE events classified as tension, shear and mixed modes of cracking based on the parametric analysis of AE waveforms, using AF vs RA values. (b) $\mathbb{FP}$ (r) and $\mathbb{FP}$ (θ) values indicated on Y-axes on left and right, respectively, of the corresponding events. (c) Timing of AE events during P1–4 and subdivided into the four constituent parts of the freeze–thaw cycles (freeze, freeze-to-thaw transition, thaw, and thaw-to-freeze transitions).

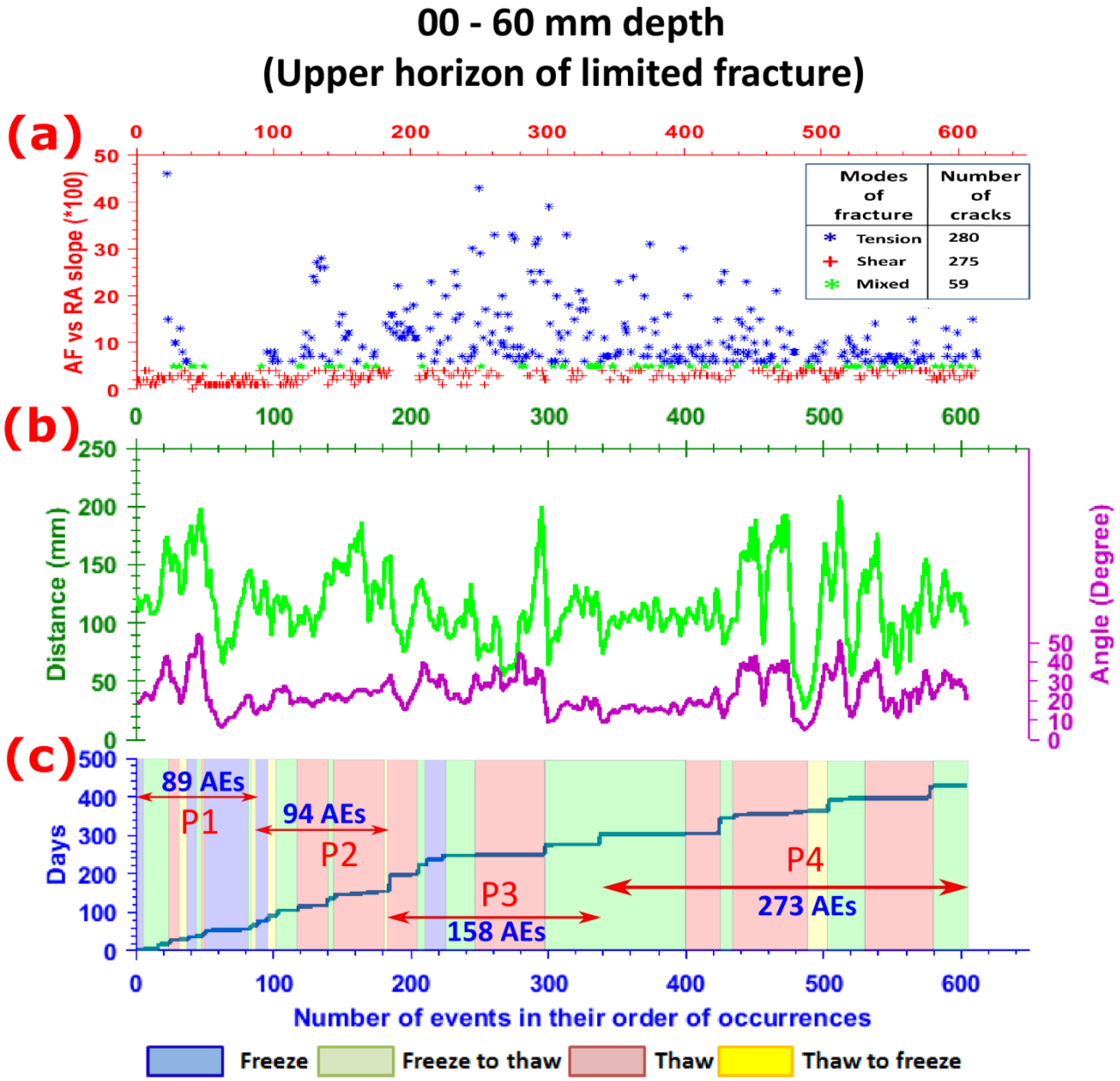

Figure 12. AE events within the 0–60 mm depth interval arranged in their order of occurrence during the four phases (P1–4) of the experiment. (a) AE events classified as tension, shear and mixed modes of cracking based on the parametric analysis of AE waveforms, using AF vs RA values. (b) $\mathbb{FP}$ (r) and $\mathbb{FP}$ (θ) values indicated on Y-axes on left and right, respectively, of the corresponding events. (c) Timing of AE events during P1–4 and subdivided into the four constituent parts of the freeze–thaw cycles (freeze, freeze-to-thaw transition, thaw, and thaw-to-freeze transitions).

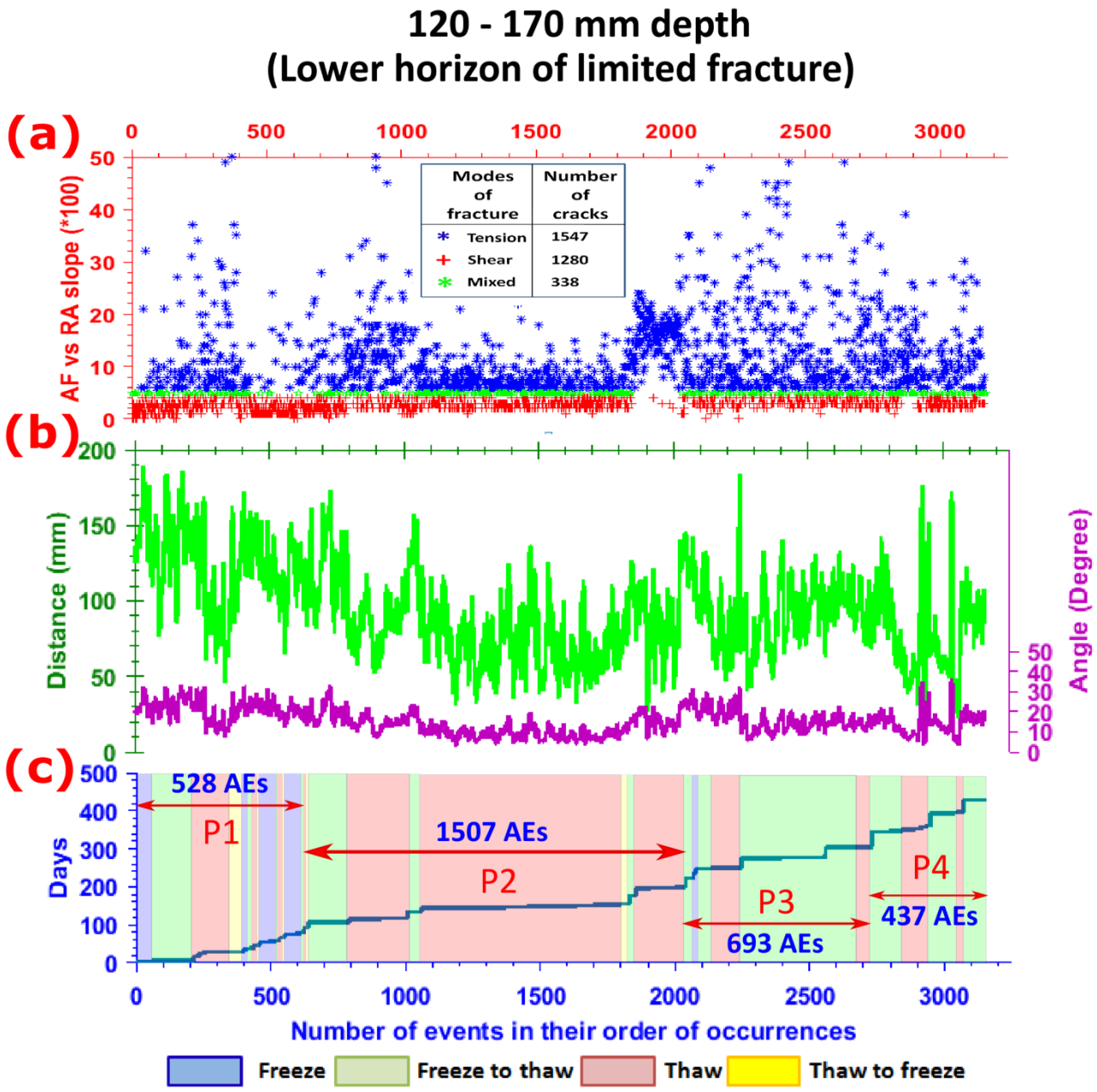

Figure 13. AE events within the 120–170 mm depth interval arranged in their order of occurrence during the four phases (P1–4) of the experiment. (a) AE events classified as tension, shear and mixed modes of cracking based on the parametric analysis of AE waveforms, using AF vs RA values. (b) $\mathbb{FP}$ (r) and $\mathbb{FP}$ (θ) values indicated on Y-axes on left and right, respectively, of the corresponding events. (c) Timing of AE events during P1–4 and subdivided into the four constituent parts of the freeze–thaw cycles (freeze, freeze-to-thaw transition, thaw, and thaw-to-freeze transitions).

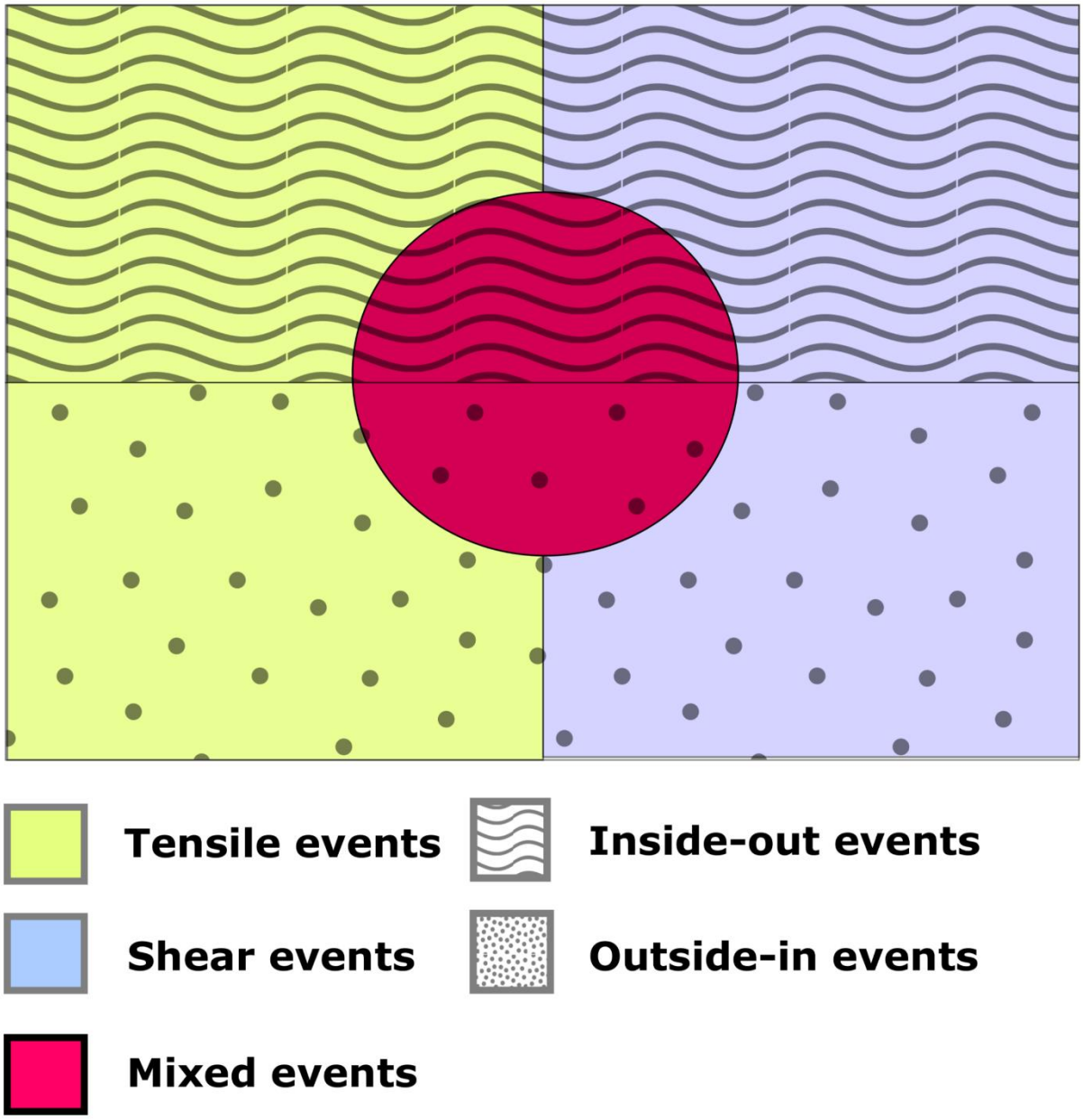

847
848 **Figure 14**. Venn diagram illustration of various conventional modes of cracking (tension, shear and
849 mixed) along with the proposed boundary situations of crack coalescence mechanisms (inside–out
850 and outside–in).

851

852 ## Supporting Information

853 Figures S1–S20.

854